

1

2 **Estimating the refractivity bias of Formosat-7/COSMIC-II**

3 **GNSS Radio Occultation in the **deep troposphere****

4 Gia Huan Pham¹, Shu-Chih Yang^{1,2}, Chih-Chien Chang¹, Shu-Ya Chen², and Chung-Yung
5 Huang³

6 ¹Department of Atmospheric Sciences, National Central University, Taoyuan, Taiwan

7 ²GPS Research and Application Center, National Central University, Taoyuan, Taiwan

8 ³Taiwan Space Agency, Hsinchu, Taiwan

9 *Correspondence to:* Shu-Chih Yang (shuchih.yang@atm.ncu.edu.tw)

10 **Abstract**

11 FORMOSAT-7/COSMIC-2 radio occultation (RO) measurements **show promise** for observing the deep
12 troposphere and providing critical information on the Earth's planetary boundary layer (PBL). However,
13 refractivity retrieved in the low troposphere can have severe **biases** under certain thermodynamic conditions. This
14 research examines the characteristics of **the deep tropospheric biases** and presents methods for estimating the
15 region-dependent **refractivity** bias using **statistical** regression models. The results show that the **biases have**
16 characteristics that vary with land and oceans. With substantial correlation between local spectral width (LSW)
17 and bias, the LSW-based bias estimation model can explain the general pattern of the refractivity bias, but with
18 deficiencies in measuring the bias in the ducting regions and certain areas over land. The estimation model
19 involving the relationship with temperature and specific humidity can capture the **large biases** associated with
20 ducting. Finally, a minimum variance estimation that combines the **LSW and temperature/water vapor models**
21 provides the most accurate estimation of the refractivity bias.

22 **1 Introduction**

23 Global Navigation Satellite System (GNSS) radio occultation (RO) observations have become a critical
24 data source in atmospheric applications, particularly numerical weather prediction (NWP) (e.g., Healy, 2008;
25 Rennie, 2010; Cucurull et al., 2007, 2017; Lien et al., 2021). Low-Earth-orbiting (LEO) satellites receive radio
26 signals from GNSS transmitters, **which tend to** bend due to atmospheric density changes. Information on the
27 bending angle can be obtained with the GNSS RO technique, and then the atmospheric refractivity is further
28 derived by Abel inversion. Since the RO technique measures the signal phase delay, it is not affected by clouds
29 and rainfall. The RO profile is an all-weather observation with a high vertical resolution.

30 The RO observations, bending angle and refractivity, **measure vertical gradients** in atmospheric density, a
31 function of temperature, moisture and pressure (Kuo et al., 2004). RO observations provide information on
32 temperature (stratosphere and upper troposphere) and moisture (lower troposphere) with low noise and low
33 systematic errors (**biases**), which **makes them useful** in atmospheric research (Eyre, 2008). Several GNSS RO
34 missions, e.g., the FORMOSAT-3/Constellation Observing System for Meteorology, Ionosphere, and Climate
35 (FS3/C), FORMOSAT-7/COSMIC-2 (FS7/C2), Meteorological Operational satellite (MetOp), Gravity Recovery
36 And Climate Experiment (GRACE), Satellite de Aplicaciones Científico-C (SAC-C), X-band TerraSAR satellite
37 (TerraSAR-X), Korea Multi-Purpose Satellite-5 (KOMPSAT-5), etc., have provided much RO data for NWP.

38 Many studies have illustrated the positive impact of assimilating RO observations, such as the operational forecast
39 systems at the European Centre for Medium-Range Weather Forecasts (ECMWF) (Healy, 2014), the
40 NCEP/Environmental Modeling Center (EMC) (Cucurull, 2007) and the Taiwan Central Weather Administration
41 (CWA) (Lien et al., 2021). Moreover, studies have been initiated recently to investigate the potential of
42 assimilating the large volume of commercial RO data from Spire, and the benefits can be identified in weather
43 forecasting (Bowler, 2020a). In addition to improving global NWP, studies have also confirmed that assimilating
44 RO observations improves severe weather prediction, particularly for tropical cyclones and heavy rainfall (e.g.,
45 Chen et al. 2020; 2021a,b, 2022; Chang and Yang, 2022; Yang et al., 2014).

46 As the successor of FS3/C, the FS7/C2 mission was launched in 2019 with support from the Taiwan
47 National Space Agency (TASA) and the United States National Oceanic and Atmospheric Administration (NOAA)
48 and National Science Foundation. The number of profiles obtained by FS7/C2 is approximately three times greater
49 than that of FS3/C since FS7/C has dense coverage over the tropics and subtropics (Chen et al., 2021c). Compared
50 with FS3/C, FS7/C2 has a higher signal-to-noise ratio (SNR), wider bandwidth, and a better open-loop (OL)
51 tracking model. These advantages enable the retrieval of more data from RO signals penetrating the moist
52 troposphere and having the ability to detect the planetary boundary layer (PBL) and superrefraction (SR) over the
53 top of the PBL (Schreiner et al., 2020). Chen et al. (2021c) showed that the data availability of the FS7/C2 RO
54 profiles under 1km is five times greater than that of the FS3/C profiles over a six-month range. Anthes et al. (2022)
55 noted that the penetration rate of RO profiles is high even under extremely moist conditions and near tropical
56 cyclones. The ability to penetrate deep into the atmosphere makes RO measurements ideal for studying the PBL.
57 The PBL is directly influenced by any exchange of energy, momentum and mass between Earth's surface and the
58 atmosphere, and thus its characteristics are crucial for weather and climate variabilities.

59 However, the use of GNSS RO in the lower atmosphere still has errors when radio rays pass through areas
60 with strong vertical or horizontal refractivity gradients. The implementation of open-loop tracking (Sokolovskiy,
61 2001) and the use of the holographic retrieval method largely reduce the negative refractivity bias (REFB) in
62 lower troposphere in earlier generation RO missions. The "radioholographic" methods such as the canonical
63 transform (CT) method (Gorbunov, 2001, 2002), Full Spectrum Inversion (FSI) (Jensen et al, 2002) and Phase
64 matching (PM) (Jensen et al, 2004) largely solve the multipath issue resulting from the "strong" refractivity
65 gradient. Still, negative REFB can arise in deep troposphere from multiple causes, as summarized by Feng et
66 al. (2020) and Wang (2020). A common cause (but not the only one) of negative biases in the lower troposphere
67 is ducting (Sokolovskiy 2003; Ao et al. 2003; Xie et al. 2010). When the vertical gradient of refractivity $\partial N/\partial z$
68 exceeds a critical value of -157 N units per km (Lopez 2009), ducting occurs and rays are trapped inside the
69 ducting layer. In the presence of ducting, the singularity problem in the Abel transforms leads to a non-unique
70 inversion problem. Thus, the Abel inversion results in a negatively bias refractivity below the ducting layers
71 (Sokolovskiy, 2003). Feng et al. (2020) reported that climatological locations agree well with the areas of high
72 ducting frequency, mainly over the subtropical eastern oceans. Furthermore, there are non-ducting related biases
73 exist in the RO data. Error associated with low SNR in the complex moist lower troposphere may cause negative
74 biases in bending angles and refractivity. Another potential source is the propagation of radio waves in a medium
75 with random refractivity irregularities can also cause biases (Gorbunov et al. 2015). In regard to the assimilation
76 of RO data, quality control (QC) is applied to reject the RO data if the observation or the corresponding

77 backgrounds are suspected to be affected by superrefraction. The rejection rate is high below 2 km due to the
78 negative bias, which could also discard valuable information for data assimilation. To increase the value of RO
79 data in the lower atmosphere, this study aims to examine the characteristics of the REFBs with the FS7/C2 RO
80 data in more detail and proposes methodologies to estimate them.

81 Previous research has demonstrated that the negative REFB in the ABL can be recognized and estimated
82 using canonical transform approximations (Sokolovskiy, 2003) and can be reconstructed in the presence of ducting
83 conditions (Xie et al., 2006). Based on Xie et al. (2006), Wang et al. (2017) developed an optimal estimation of
84 negative bias using precipitable water (PW) observations from Advanced Microwave Scanning Radiometer from
85 the EOS (AMSR-E) microwave radiometer satellite data. Wang et al. (2020) further proposed a bias estimation
86 algorithm by generating a candidate set of modeled ducting profiles. The one with the vertical gradient of the
87 reflected bending angle closest to the observed profile is taken as the bias-corrected profile. However, there are
88 some limitations with these methods, such that they only correct for ducting-related bias and the grazing signal of
89 the bending measurement is needed. For the RO observation error, the local spectral width (LSW), which measures
90 the uncertainty of the RO bending angle, has been used to indicate the quality of the individual RO profiles. The
91 LSW represents the errors caused by the nonspherical symmetry of refractivity in the moist troposphere
92 (Gorbunov, 2006; Sokolovskiy 2010). The LSW parameter has improved the use of RO observations in data
93 assimilation, including in the QC procedure (Liu et al., 2018) and dynamic estimation of RO error in the lower
94 troposphere (Zhang et al. 2023). Liu et al. (2018) showed that both uncertainties and biases were related to LSW.
95 Sjoberg et al. (2023) recently showed a strong statistical correlation between lower tropospheric uncertainties and
96 LSW. They also mentioned that they found a correlation between biases and LSW as well, but did not provide
97 details. Furthermore, Bowler (2020b) proposed estimating RO errors with information on mean temperatures
98 below 20 km. These results suggest that variations in LSW, temperature and humidity are related to the bias. Thus,
99 we developed statistical models that adaptively consider the biases associated within each RO profile using LSW
100 and temperature and water vapor.

101 We first investigate the characteristics of the FS7/C2 RO REFB and establish regression-based bias
102 estimation algorithms. Two types of algorithms are examined. One is based on the physical LSW parameter, and
103 the other is related to thermodynamic variables (temperature and water vapor). By comparing the results of the
104 estimated bias, we can identify how they link to the characteristics of each participating variable. Finally, a bias
105 correction method for the RO profile in the lower troposphere is proposed by combining the two error estimation
106 algorithms. We expect that this new algorithm can be used in different aspects such as improving the products of
107 temperature and moisture profiles retrieved from the refractivity in the moist lower troposphere (Chen et al. 2020),
108 definition of the PBL height (Xie, 2014), and the estimation of precipitable water vapor (Yeh et al. 2024).
109 Furthermore, for the DA systems that assimilate the RO refractivity, it is expected that the RO data in the deep
110 troposphere can be better exploited by using the bias estimation as a QC flag or assimilating the calibrated
111 refractivity profiles.

112 The remaining portions of this paper are organized as follows. Section 2 provides the data information and
113 methods for estimating the refractivity bias. Section 3 discusses the general characteristics of bias and its
114 sensitivities with respect to different variables and land/sea conditions. Section 4 presents the results of bias
115 estimation algorithms. Finally, the summary and conclusion are provided in Section 5.

116 2. Data and methodology

117 2.1 GNSS RO FS7/C2 and ECMWF data

118 This study uses the FS7/C2 RO atmospheric profiles (atmPrf) and wet products (wetPf2) processed by
119 the Taiwan Data Processing Center (TDPC). The study period is from 1st December 2019 to 29th February 2020,
120 before the FS7/C2 data were assimilated in the ECMWF analysis. All RO profiles are distributed between 45°S
121 and 45°N due to the low inclination orbits of the FS7/C2 satellites. A total of 244,853 profiles are selected
122 with the flag of “good data” during the periods, and only data below the height of 25 km are used to focus on the bias
123 characteristics in the troposphere. The data quality of the FS7/C2 constellation is improved compared to
124 FS3/COSMIC (FS3/C) due to the use of the advanced RO receiver and postprocessing with open-loop tracking.
125 Most of the profiles show a deeper penetration with depths below 1 km, and the penetration rate is 40% higher
126 than those of FS3/C (Chen et al., 2021c). Figure 1 shows the number of profiles that penetrate below 1.5 km
127 above the mean sea level (MSL) during the selected periods. The FS7/C2 data are mostly in tropical areas and have more
128 profiles penetrating below 1.5 km over oceans than over land.

129 The ECMWF atmospheric reanalysis (ERA5, [https://www.ecmwf.int/en/forecasts/access-forecasts/access-](https://www.ecmwf.int/en/forecasts/access-forecasts/access-archive-datasets)
130 [archive-datasets](https://www.ecmwf.int/en/forecasts/access-forecasts/access-archive-datasets)) is used as the reference RO profiles. The hourly ERA5 reanalysis in the study period has a
131 horizontal resolution of 0.25 x 0.25 deg with 37 pressure levels, ranging from 1000 to 1hPa. The variable
132 geopotential, temperature and specific humidity are selected. Since the time of the RO data is precise in minutes,
133 we rounded the time of the RO profiles to the nearest hour. The ERA5 profiles are derived by interpolating the
134 reanalysis horizontally and vertically to the location and vertical levels of the RO atmPrf. The RO REFB is defined
135 as the difference between the FS7/C2 and the ERA5 RO observations at each level. This assumes that the ERA5
136 refractivities are close to truth. These biases are referred to as the real biases in this paper. Nevertheless, it is
137 possible that ERA5 may carry its own biases, which will not be discussed in this study.

138 For constructing the statistical models, the predictors are LSW, temperature (T), and specific humidity (Q).
139 The LSW, available in the atmPrf data, are calculated from the width of the spectrum during the RO processing
140 (Liu et al. 2018). The T and Q , available in the wetPf2 data, are computed from a one-dimensional variational
141 (1D-Var) retrieval algorithm using ECMWF 12-h forecast as the a priori (Wee et al. 2018).

142

143 2.2 Statistical models for bias estimation

144 Two polynomial regression models are developed to estimate the REFB using predictors associated with
145 different attributions of the observational error in GNSS RO data. The first model uses LSW/2 as the predictor,
146 and the other uses temperature (T) and specific humidity (Q) as the predictors. Liu et al. (2018) used a linear
147 function of LSW/2 to illustrate the FS3/C dynamic error variance in the bending angle and refractivity, and the
148 scaling factor 1/2 for LSW approximates the root mean square of random error of the bending angle (Liu et al.
149 (2018), assuming a Gaussian spectrum (Sirmans and Bumgarner 1975). Following Liu et al. (2018), we use the
150 variable LSW/2 and modify this relationship to a polynomial regression. The other bias estimation model is
151 established using the thermodynamic variables to emphasize the impact of the thermodynamic structure on REFB
152 in deep troposphere. The two polynomial regression models are referred to as the LSW and TQ estimators,
153 respectively. The LSW represents the RO inversion uncertainty, and T and Q represent the impact of the

154 thermodynamic structure on REFB within the ABL. Each of these variables is expected to partly explain the
155 characteristics of the bias.

156 In each estimator, the order of the polynomial and regression coefficients are optimized by using the metrics
157 of R-squared and mean square error to assess the goodness of the fitting performance. The polynomial regression
158 is performed with the training data, which is 80% of the total data, and the rest (20%) of the data is used for
159 evaluating the regression performance. To derive a robust regression model, independent regression fitting is
160 repeated five times by replacing the training/testing data with a different 80%/20% subsets of the data so that the
161 testing data from five experiments eventually covers the whole data set. The regression model with the best fitting
162 performance for both training and testing data is chosen as the optimal one. Given that our goal is to construct
163 regional-dependent estimators to consider the spatial variation in the REFB, we group the RO refractivity profiles
164 from 45°S to 45°N into 5°longitude x 3° latitude boxes (Figure 1), and the regression-based REFB estimators are
165 built in each box. In total, there are 72 x 30 boxes. The boxes are defined by considering the number of available
166 RO profiles below 1.5km should be at least 10 profiles in each box for conducting the regression training and
167 testing. With the 3 months of data used in our study, choosing testing data lower than 20% of the total data results
168 in a very coarse resolution of the boxes. On the other hand, choose any number larger than 20% would sacrifice
169 the amount of data that can train a reliable regression model. We note that all profile data below 1.5 km are used
170 first (80% for training and 20% for testing) to determine the order of the LSW-based regression model and the
171 optimal combination of the multi-variable (T and Q) regression model.

172 For the LSW estimator, a second-order polynomial is chosen based on the R-squared metric. Afterwards, a
173 second-order polynomial regression is constructed for an individual box. Eq. (5) shows the formula of the LSW
174 estimator in the i^{th} box

$$175 \quad u_i = \alpha_{i,1}x_i^2 + \alpha_{i,2}x_i + \alpha_{i,3} \quad (1)$$

176 where u_i , the predictand, is the REFB, x_i is the LSW/2, and $\alpha_{i,*}$ are the regression coefficients. Although the
177 biases related to the signal tracking or multipath is much reduced after with the implementation of open-loop
178 tracking and radio-holographic retrieval method, we expect that LSW can partially capture the biases inherited
179 from bending angle.

180 A similar procedure is applied to derive a multivariable polynomial regression model with T and Q obtained from
181 the 1D-Var analysis of the RO wet products (Wee et al. 2018) as the predictors. For consistency, the real REFB
182 originally defined with the atmPrf, will be interpolated to the same levels of the wetPf2. No REFB, T and Q are
183 collected if the T , Q profiles terminate above 1.5 km MSL. Before fitting, T and Q are standardized as

$$184 \quad \chi = \frac{x_i - \min(x_i)}{\max(x_i) - \min(x_i)} \quad (2)$$

185 where χ represents a normalized quantity ranging between 0 and 1 and x_i is the original value of Q or T in the i^{th}
186 box. Given two variables, there are different combinations of order and interaction terms (multivariable
187 polynomial function has the form of $\sum_{m=0}^M \sum_{l=0}^L b_{m,l} y^m z^l$, where m and l are the order of variable y and z ,
188 respectively, and $b_{m,l}$ is the regression coefficient). For this application, the mean squared error is used to
189 determine the optimal fitting formula given that R-squared are comparable when higher order terms are included.
190 The optimal multivariable polynomial regression model has the form:

191
$$u_i = \beta_{i,1}y_i^2 + \beta_{i,2}y_i + \beta_{i,3}y_iz_i \quad (3)$$

192 where u_i is REFB, y_i is the normalized Q , z_i is the normalized T and $\beta_{i,*}$ are the regression coefficients.
 193 Considering the quadratic term of moisture is essential. The R-squared (MSE) value increases (decreases) from
 194 0.535 (37.044) with the y_i and y_iz_i terms to 0.732 (26.610) with the y_i^2 term.

195 We further apply the minimum variance estimation (MVE, Clarizia et al., 2014) to combine the results
 196 from the LSW and TQ estimators. This approach has the advantage of having a smaller RMS error than either the
 197 LSW or TQ estimation. The MVE is built to linearly combine the estimations so that the new estimation has the
 198 minimum error variance:

199
$$u_{i,MVE} = \mathbf{m} \cdot \mathbf{u} \quad (4)$$

200 where \mathbf{u} is the vector of individual estimated refractivity bias and \mathbf{m} is the vector of combination coefficients. One
 201 of the advantages of this combination is that \mathbf{m} is derived considering the error covariance matrix of individual
 202 bias estimators.

203
$$\mathbf{m} = \left(\sum_{i=1}^K \sum_{j=1}^K c_{i,j}^{-1} \right)^{-1} \mathbf{C}^{-1} \mathbf{1} \quad (5)$$

204 where $\mathbf{1}$ is a vector with all elements equal to one, K is the dimension of \mathbf{m} ($K = 2$ in our application), \mathbf{C}^{-1} is the
 205 inverse of the covariance matrix between the individual estimation errors and $c_{i,j}^{-1}$ are the elements of \mathbf{C}^{-1} .

206 The element of the error covariance matrix \mathbf{C} is expressed as $c_{ij} = \langle (\mathbf{u}_i - \mathbf{u}_t)(\mathbf{u}_j - \mathbf{u}_t) \rangle$, where u_i and u_j is the
 207 i^{th} and j^{th} bias estimation, respectively, and u_t is the real bias.

208 3 Characteristics of the refractivity bias

209 3.1 General characteristics of REFB

210 Figure 2a shows the profile of the averaged REFB and its standard deviation from 0-25 km. RO data have
 211 significant biases in comparison to the ERA5 reference, especially in the low troposphere. The bias is evident
 212 below 5 km and is largest at the surface with an amplitude of approximately -11 N-units. Given the large variations
 213 in moisture and temperature in the low troposphere, the standard deviation below the 2 km height increases as the
 214 height decreases. Notably, although the total number of profiles quickly decreases below 5 km (Fig. 2b), there
 215 remain enough data for near-surface statistical evaluation, with about a 40% penetration rate at 0.5 km in reference
 216 to the total number of profiles at 10 km (Fig. 2c). The mean LSW (red line in Fig. 2a) also increases sharply as
 217 the height decreases, with two peaks, at the surface and near 2 km.

218 Figure 3a shows the latitudinal cross-section of the REFB. The largest values of REFB are below 5 km in the
 219 subtropics and tropics and slightly shifted to the Southern Hemisphere due to the austral summer. The opposite
 220 pattern, which has a high bias shifted to the Northern Hemisphere, is also seen with the data from June to August
 221 2020 (not shown). This result indicates the general dependence of the distribution of REFB on the seasonal
 222 temperature and water vapor structure. Similar to the REFB pattern, large LSW occurs mainly in the tropics, tilting
 223 toward the Southern Hemisphere with the maximum near the surface (Fig. 3b). This finding illustrates that LSW
 224 variation can be related to the REFB to some extent. Moreover, other high LSW values are located a few

225 kilometers above the surface of the Southern Hemisphere. The increased LSW above 2 km could be caused by
226 common inversion layers in the troposphere of some oceans (Sokolovskiy et al. 2014). Another effect that could
227 be considered is the influence of convective clouds just above moist oceans (Yang et al., 2016). The large LSW
228 near the surface in Fig. 3b reflects the ability of FS7/C2 to penetrate deep into the moist troposphere of the tropics.
229 However, this surface maximum was not seen in the study of Zhang et al. (2023) using FS3/C data in August
230 2008.

231 3.2 Dependence on geography and thermodynamic conditions

232 We further examine the dependence of the REFB on land and oceanic thermodynamic conditions. Figure 4
233 compares REFB between land and ocean, together with its standard deviation (stdv) and LSW. Both REFB and
234 LSW below 4 km are somewhat larger over oceans, and the REFB extends to higher altitudes (Fig. 4c vs. 4d) with
235 a greater vertical gradient of REFB below 2 km. The magnitudes of mean REFB and stdv above 2 km are
236 comparable over land and ocean. The shape of the LSW profiles is different over oceans and land, with the second
237 peak value at 2 km more pronounced over oceans. Below 1.5 km, the shape of the REFB profile exhibits
238 characteristics as the LSW profiles, suggesting the potential of LSW as a predictor for estimating REFB.

239 Given the large REFB in deep troposphere, we focus on the regional variations in REFB averaged below 1.5
240 km. Figure 5a shows that the averaged value of negative REFB below 1.5 km is largest over the oceanic regions
241 near the western coasts of the South American and African continents. Small negative REFBs appear over the
242 tropical Pacific and land. There are small positive REFBs over the high mountain regions. The different behavior
243 of the REFB over ocean and land implies the impact of regional variability and the associated thermodynamic
244 structure in the lower troposphere. As shown in Fig. 5b-5d, high LSW occurrence is mainly located over the warm
245 equatorial regions of the Pacific, Atlantic and Indian Oceans. However, not all of the regions with high temperature
246 and moisture coexist with the regions with high LSW. Some exceptional regions can be seen, such as offshore to
247 the coast of Southwest Australia and offshore of Southwest Africa near the international data line. Fig. 5 suggests
248 that although LSW, temperature and specific humidity have certain cross-relationships, the characteristics of
249 thermodynamic conditions cannot fully explain the distribution of LSW. Therefore, an REFB estimation model,
250 which is based on only one variable, is not enough to explain REFB.

251 To further highlight the characteristics of REFB under different conditions, the REFB profiles are grouped
252 according to each profile's LSW, temperature and specific humidity averaged below 1.5 km for land and ocean
253 (Figure 6). As Xie (2014) reported, the 1.5 km MSL is the global mean PBL height calculated from the FS3/C
254 refractivity data. In general, it is evident that the negative REFB increases with increasing LSW below 4 km, as
255 shown in Fig. 3; however, the characteristics are different for land and ocean. Over land, the very high LSW does
256 not guarantee the occurrence of a large REFB in lower troposphere. Moisture and temperature likewise exhibit
257 the same linear relationship with negative REFB in the lower troposphere. However, negative REFBs also tend to
258 occur under conditions of low moisture over the ocean. Figure 6 reveals that the relationship between REFB and
259 LSW, T and Q under 1.5 km is dominantly linear; however, the REFB variations can be further explained by a
260 quadratic relationship with Q . It is noted that REFB at about 10 km increase with increasing LSW, T and Q over
261 both land and oceans, and even become weakly positive at high values of LSW, T and Q averaged below 1.5km.
262 In particular, RO profiles over land with large LSW below 1.5km has the largest positive REFB, nearly 8 N-unit,

263 aloft. Taking only the RO profiles penetrating 0.5 km will modify the characteristics of Figure 6 in two aspects.
264 First, the REFB below 10 km becomes positive for LSW/2 larger than 28%. Second, the REFB for cold
265 temperature shows negative at 15 km. The former feature is related to the early cutoff height in the tropical
266 occultation over central Africa (Sokolovskiy, 2010). The latter feature is attributed to the inversion associated with
267 the large-scale subsidence near the tropopause near mid-latitude. Sensitivity tests to address sampling issues will
268 be discussed in subsection 4.2.

269 4 Results of bias estimation

270 4.1 General performance

271 In this section, we present the estimation for REFB using the methods introduced in Section 2. As
272 mentioned, LSW/2, which represents the retrieval uncertainties of the bending angle and, hence, refractivity
273 uncertainties, is the predictor for the first bias estimation model. The T and Q retrieved from FS7/C2 RO data are
274 the predictors for the second estimator. Although the T and Q products retrieved from RO profiles using 1D-Var
275 retrievals may have errors, they still provide valuable information for REFB estimation through the training
276 process, as described in Section 2.

277 Figure 7 shows the relationship between the REFB and LSW/2 averaged below 1.5 km for the Southern
278 Hemisphere (SH) and Northern Hemisphere (NH). REFB is grouped every 2% of LSW/2, from 0 to 36%. The
279 solid and dashed lines show the LSW-based REFB estimates for ocean and land, respectively. Under 1.5 km, the
280 magnitude of the negative REFB as a function of LSW is larger over oceans than for land. Generally, as LSW/2
281 increases, the REFB becomes more negative below 1.5 km for both land and ocean. Although the relationship is
282 dominated by a linear trend, the quadratic term further improves the regression fitting. As shown in Table 1, the
283 correlations over ocean and land are robust (larger or close to 0.9) and similar with the training and testing data
284 in SH and NH. Compared to the REFB under the warm and moist condition of the austral summer in SH, the
285 REFB over NH is weaker but the relationship between LSW/2 and REFB is still strong over ocean and land,
286 except that the one over land has a somewhat stronger quadratic feature. Given this strong relationship, we expect
287 that the relationship during the boreal summer season will hold as well. However, the relationship between REFB
288 and LSW/2 is not present above 1.5 km, and there is little difference in REFB between land and ocean.

289 Figure 8 shows the result of the second bias estimator, which relates the REFB with normalized Q (y)
290 and product of normalized T and Q (yz) under 1.5 km. The TQ estimation over ocean and land captures the feature
291 where the REFB becomes more negative under moist conditions. Similar to the LSW estimator, the TQ estimator
292 shows a stronger dependence over the ocean. The multivariable regression has correlation coefficients equal to
293 0.79 and 0.72 for ocean and land in SH, respectively, and 0.75 and 0.69 in NH. In general, the REFB shows a
294 robust bi-linear relationship with y and yz , and the quadratic term (y^2) provides further adjustment. With a fixed
295 specific humidity, lower temperature results in larger negative REFB. In Fig. 8a, this result reflects the condition
296 over the cool SST (Fig. 5a and 5d), west of the coast of South America and South Africa. The relationship becomes
297 more linear in NH (Fig. 8a vs. 8c), i.e. less dependence to the quadratic term of specific humidity. For dryer
298 condition, the TQ estimator tends to give neutral to positive REFB, especially over land (Fig. 8b and 8d) where
299 more data are in the dry condition and part of them are over the mid-latitude continent (Fig. 5c). Given a fixed TQ

300 value ($\nu_z=0.5$) in Fig. 8, Figure 9 shows the strong relationship between REFB and Q . Large negative REFB
301 corresponds to moist condition, but the negative amplitude is larger over the SH ocean with larger variation. The
302 relationship is more quadratic over ocean than over land and is most linear over the NH land. In Figure 8, a slightly
303 positive REFB is estimated for very cold and dry condition over ocean. In Feng et al. (2020), positive REFB is
304 identified in Bering Ocean at high latitude. While Fig. 8 qualitatively suggests the potential to capture such
305 positive REFB over high-latitude, whether the regional-dependent TQ estimator can be adequately applied to
306 estimate REFB in the polar or high-latitude regions is still an open question since the FS7/C2 data RO data used
307 in this study mostly distributed in the tropic to subtropic regions.

308 Figures 7 and 8 confirm that models with LSW/2 or TQ as predictors can estimate the REFB under 1.5 km, but
309 there are different sensitivities for ocean and land. In the next step, we further apply these regression methods
310 using the data in 5° longitude \times 3° latitude boxes within 45° N to 45° S to construct the region-dependent bias
311 estimation model.

312 Figure 10 shows the horizontal distribution of the mean real and estimated REFBs with the training and
313 testing data. Notably, there are some differences between the training and testing data (Fig. 10a vs. 10b), such as
314 the large REFB off the western coast of South American and coast of Australia. In comparison to the real REFB
315 distribution (Fig. 10a), the LSW-based REFB (Fig. 10c) captures the general pattern with larger biases over ocean
316 and lower biases over land in both the training and testing data. However, the LSW-based REFB is less capable
317 of capturing the large bias over the subtropical oceans off the west coast of South America and South Africa and
318 Australia. Those are expected to be the oceans that have a cold SST, where ducting occurs commonly due to the
319 frequent occurrence of inversion layers on top of the cool sea surface. Although the LSW-based REFB can also
320 represent a portion of the negative REFB in these regions in general, it is obvious that the values are
321 underestimated there. The LSW-based estimation exhibits good performance in estimating the negative REFB in
322 the Indian Ocean, where the pattern and magnitude of the estimated REFB are close to those of the real REFB. In
323 contrast to the LSW-based REFB, the TQ -based REFB represents the large negative REFB in the high-ducting-
324 occurrence regions well. Although the magnitude of the N -REFB offshore the coasts of South America and South
325 Africa is still underestimated, the pattern and amplitude of the negative REFB are much better represented in
326 comparison with the LSW-based estimation.

327 The TQ -based estimation (Fig. 10 e,f) captures the low bias pattern well, such as the tropical western
328 Pacific, western South America and Africa, while the LSW-based estimation overestimates the negative bias. The
329 similar pattern between the real and TQ -based estimated REFBs can be explained by the following two reasons.
330 The first reason is the ability to capture SST characteristics. For example, cold SST regions can result in a cool,
331 low moisture near-surface atmosphere (Fig. 5c and 5d) and impact the boundary layer. Second, the bias in the RO
332 refractivity profiles will be translated to the 1D-Var T and Q retrievals.

333 The final method, the MVE, combines the LSW and TQ estimations. As described in Section 2, the MVE
334 derives the optimal combination by considering the error correlation between the individual estimations. Notably,
335 the MVE approach requires knowledge of the error covariance matrix between two components (the matrix C in
336 Eq. 5). The error correlation of the two REFB estimators is 0.294. A high error correlation indicates a dependency
337 between the two components and thus there is less benefit from using the MVE method. Although LSW is known

338 to have a relationship with **temperature and water vapor**, our results indicate that the error correlation between
339 two estimates is low enough that it is expected that the MVE can extract useful information from both estimations.
340 Compared to the LSW and ***TQ* REFB** estimation, the results of the MVE show a pattern closer to the real REFB
341 with both the training and testing data sets.

342 **We next show** the root-mean-square error (RMSE) between the real and estimated REFB in each box.
343 Figure 11 shows the contribution of each estimation in estimating bias for land and oceans and reflects the
344 representativeness of the mean REFB shown in Fig. 10. The LSW-based estimation exhibits high RMSE in the
345 cold SST regions and several ocean regions, such as the Southeastern Atlantic, Southeastern and North Western
346 Pacific Oceans, while the ***TQ*** estimation successfully mitigates this issue. On the other hand, the LSW-based
347 estimation performs better in the tropical Atlantic and Indian Oceans. **With training and testing data, the large**
348 **RMSEs in the LSW or *TQ* estimation over the oceans are largely removed by the MVE method; however slight**
349 **degradation is observed over the continents of south America and middle Africa.** With the testing data (**the right**
350 **column in Fig. 11**), the RMSEs are larger in individual estimations, as expected. **In general**, the MVE method
351 retains its advantage in the optimal estimation **over ocean**, with an RMSE smaller than that of either estimation.
352 Table 2 shows the global mean RMSE. The ***TQ*** method has a smaller RMSE compared to the LSW estimation.
353 The MVE method further improves the ***TQ*** method by 32% and 23.6% with the training and testing data,
354 respectively.

355 **However, we also observed that the *TQ*-based REFB has larger RMSE in the ducting region in southeast**
356 **Pacific and Atlantic (Fig. 11e vs. Fig. 11f).** This is attributed to an overestimated negative REFB (Fig. 10e vs.
357 10f) by the ***TQ*** estimator with a much moister near-surface condition in the testing data than those in the training
358 data. The overestimation of the testing data in the ducting regions suggests that more data is required to train the
359 statistical model applicable to a broader range of temperature and moisture requires.

360 **4.2 Sensitivity experiments**

361 This subsection discusses the sensitivity of the REFB estimation to the penetration rate of the RO profiles
362 and investigate the impact of sampling error on constructing the LSW-based and ***TQ***-based estimators. Two sets
363 of sensitivities are designed. For the first set of sensitivity, it is required that, in each box, at least 30 RO profiles
364 penetrate a certain level. For the second set of sensitivity, the REFB estimators are obtained for RO data from
365 different levels.

366 Figure 12 shows the REFB estimation with the testing data using different criteria of the penetration rate.
367 The estimators are obtained when there are at least 30 profiles whose minimum level is smaller than 1.5 or 0.5
368 km, respectively. The criteria are referred to as CT1 and CT2 in Fig. 12. As the criterion becomes more stringent,
369 more samples in the tropics are rejected and insufficient samples are available in the core of the ducting regions
370 and areas with latitudes higher than 30 degrees. For boxes with sufficient samples with the CT2 criterion, the
371 patterns of REFB, LSW, ***T*** and ***Q*** (the right column in Fig. 5) are very similar to the ones with an eased standard
372 criterion, but their amplitudes are generally higher. Nevertheless, the real REFB in Fig. 12a and Fig. 12b is very
373 similar to that in Fig. 10b using an eased criterion on sample number. This similarity is due to fact that the data
374 amount between 0.5 and 1.5 km is much more than that below 0.5km (Fig. 2b). However, the real REFB with
375 CT2 is larger in south Pacific and Atlantic. This reflects that the REFB quickly increases near the surface (Fig. 3a),
376 which can be emphasized after the RO profiles with early termination are removed. The LSW-based REFB with

377 strict criteria also captures the general pattern of real REFB, while the *TQ*-based REFB captures the large negative
378 REFB in the ducting regions well. The REFB estimation using the C2 criterion still show good ability in the
379 regions that the real REFBs are somewhat different between the C2 and standard criteria, such as Central and
380 northwestern Pacific. This good performance is attributed to the fact that the region-dependent regression models
381 can adapt to the changes in the training data in boxes.

382 Based on the results in Fig. 12, we separate the REFB estimation to different vertical levels, below 0.5
383 and between 0.5 and 1.5 km (Figure 13). As shown in Fig. 3b, the real REFB below 0.5 km is generally larger
384 than that between 0.5 and 1.5km, except for western Pacific and the ducting regions, west of south America and
385 south Africa. Below 0.5km, the penetration rate declines quickly, reducing the sample size. Nevertheless, it is
386 shown that both REFB estimators perform well in estimating the REFB as well, in particular that the *TQ*-estimator
387 is good at capturing the large REFB. Both estimators can even capture the large negative REFB in central southern
388 Pacific and south India, and the MVE REFB improves the *TQ*-based REFB in central Pacific (150°W to 150°E).
389 However, the *TQ*-estimator provides positive REFB estimation in the cold and dry condition north of Africa, while
390 a weak negative value is exhibited in the real REFB. While the *TQ*-estimator is very sensitive to the amplitude of
391 temperature and moisture, we emphasize that the regression model may not be reliable with a limited sampling
392 size in mid-latitude regions. Results of the REFB estimation between 0.5 and 1.5 km are very similar to Fig. 10.
393 This again confirms that the REFB shown in Fig. 10 is dominated by the data between 0.5 and 1.5 km.
394 Nevertheless, it is important that both REFB estimators can reflect not only the general characteristics and also
395 the differences at different vertical levels.

396 4.3 Estimating vertical profiles of refractivity bias

397 This section examines the performance of the REFB estimation methods and whether they can be used
398 for estimating the vertical profiles of REFB. The following three areas (indicated in Fig. 9a) with different REFB
399 characteristics are selected as examples: Area A is in the region of $0^\circ < \text{Lat} < 10^\circ\text{N}$ and $55^\circ\text{E} < \text{Lon} < 75^\circ\text{E}$, Area
400 B is in the region of $20^\circ\text{S} < \text{Lat} < 30^\circ\text{S}$ and $105^\circ\text{W} < \text{Lon} < 85^\circ\text{W}$, and Area C is in the region of $35^\circ\text{S} < \text{Lat} <$
401 45°S and $120^\circ\text{W} < \text{Lon} < 135^\circ\text{W}$. For each area, the estimated REFB at different levels are derived using the
402 estimation methods defined in the previous section. Figure 14a-c shows the mean of the real and estimated REFB
403 profiles in three areas with the testing data. We note that the results of the training and testing data are very
404 similar. In Area A, the mean negative REFB is large at the surface but gradually reverses to a positive bias at 3
405 to 5 km. In this case, the air below 2 km is very warm and moist over the Indian Ocean (Fig. 14d). The highly
406 humid condition gives a large LSW (Fig. 5b and 5c), and thus, the LSW method can have a good ability to
407 estimate bias in this circumstance, while the *TQ* method overestimates the negative REFB. In contrast, Area B
408 shows different patterns (Fig. 14b): the real negative REFB is even larger (-17 N units) at the surface, and the
409 negative bias at 2 km is still large compared to that in Area A. As shown in Fig. 14d, this characteristic is
410 associated with the inversion layer at 2 km over the cold SST region and large vertical moisture gradient, a typical
411 condition of ducting. While the LSW-based estimation underestimates the negative REFB with the existence of
412 the inversion layers this can be captured by *TQ*-based estimation. Nevertheless, the MVE method is always much
413 closer to the real REFB. In Fig. 14b Area B shows the improvement in the MVE than the *TQ*-based estimation,
414 while large RMSE remained in Area B with the MVE method in Fig. 11f. It should be noted that Fig. 11 is
415 calculated based on the difference the real REFB and estimated REFB of each profile “averaged” below 1.5 km,

416 where Fig. 14 groups the profiles with an interval of 500m. Therefore, the overestimation REFB below 1km with
417 the *TQ*-based estimator is alleviated with the average data used to construct Fig. 11.

418 For the box located offshore of north America with the mid-latitude cold and dry condition (Fig. 14c),
419 both estimators capture the general pattern of the vertical distribution of REFB but the amplitude below 1 km is
420 smaller than the real REFB. Nevertheless, the *TQ*-based REFB is much better represented compared to one from
421 the LSW estimator. Fig. 14 suggest that both estimators can be applied to estimate the vertical variations of REFB
422 in different regions. However, sample issues may be encountered in mid-latitude regions as discussed in section
423 4.2.

424 5. Conclusions

425 This study investigates the characteristics of refractivity bias (REFB) of FS7/C2 and its sensitivities to RO
426 measurement uncertainty (LSW) and thermodynamic conditions (temperature and moisture). Two bias estimation
427 models are constructed based on polynomial regression with the LSW, and temperature and specific humidity are
428 used as predictors in each estimation. The study period is December 2019-February 2020, with the ERA5
429 reanalysis data taken as the reference truth.

430 Similar to previous studies, the low-level FS7/C2 RO refractivity data of during the study period contain
431 significant biases when compared with ERA5. In general, the REFB below 1.5 km is negatively proportional to
432 LSW and exhibits a stronger dependency over ocean than over land. Additionally, REFB in the PBL has a strong
433 dependence on low-level temperature and moisture. While the majority of Pacific and Indian Oceans with warm
434 SSTs have significant negative REFBs, the largest negative REFB regions are near the cold SST regions off the
435 western coasts of South America and South Africa. Small and even positive REFBs are observed over South
436 America and South Africa.

437 Two REFB estimation models based on the polynomial regression approach are first applied to construct the
438 region-dependent mean REFB below 1.5 km. One estimation model uses a quadratic function of LSW. The other
439 uses the multivariable polynomial regression with temperature and specific humidity (*TQ*) as predictors, and the
440 moisture variable become emphasized after optimization. The estimation models are then applied to 72×30 boxes
441 from 45°S to 45°N. The minimum error variance (MVE) method is used to combine two REFB estimations. The
442 results show that the bias estimation models with either LSW or *TQ* have their own advantages in estimating
443 REFB. The LSW-based model shows the ability to capture the general pattern of the negative REFB but the
444 amplitude is significantly underestimated in the ducting areas. The *TQ*-based model has great performance in
445 representing the pattern and amplitude of REFB, particularly the large negative REFB in the ducting areas and
446 small REFB over most land regions. While the relationship between REFB and LSW below 1.5km is very strong
447 in a global sense, the *TQ*-based REFB shows its advantage in capturing the regional characteristics. The MVE
448 estimation successfully adopts the advantage from either LSW or *TQ* estimation and has the smallest RMSE,
449 particular over ocean.

450 Results of sensitivity tests show that the estimators at mid-latitude could be affected by the sampling issue
451 since requiring profiles penetrating 0.5 km cannot obtain sufficient samples to construct the regression models.

452 With the 3 months of data, the REFB estimation in tropic to subtropic regions remains similar with the RO profiles
453 penetrating below 1.5 or below 0.5km given that the amount of RO data between 0.5 and 1.5 km dominates.
454 Nevertheless, both the LSW and TQ estimation can capture the characteristics of REFB when the RO data are
455 separated to below 0.5 and between 0.5 and 1.5km. Such an ability allows the three REFB estimation models to
456 be applied to reconstruct the REFB vertical profiles for regions with distinct thermodynamic condition in deep
457 troposphere. Both the LSW and TQ estimations can well represent the vertical gradient of the mean REFB and
458 the MVE estimation gives an estimated REFB profile closest to the real REFB with the probability distribution
459 similar to the distribution of real REFB.

460 We should note some of the limitations of these REFB models. The temperature and moisture from the
461 ERA5 reanalysis may have bias. In addition, factors such as temporal variations, local topography and
462 meteorological effects, are neglected in this study. The biases may have more characteristics regarding smaller
463 scales spatiotemporally. We should also emphasize that the FS7/C2 RO data are mainly located in the tropic to
464 subtropic regions. Therefore, we need more data to justify whether the regression-based bias estimation is
465 applicable in the high-latitude regions. For future work, bias estimation models will be constructed at higher
466 resolutions with more RO profiles collected from the current FS7/C2 or other operational and commercial GNSS-
467 RO satellites.

468 **Author contribution:** SY was in charge of the conceptualization of this study. SY and GP prepared the manuscript
469 with contributions from all co-authors. GP constructed the packages of bias estimation. SY and GP analyzed the
470 data. SY and GP wrote the manuscript draft; CC, SC, and CH reviewed and edited the manuscript. The authors
471 greatly appreciate Dr. Rick Anthes and the anonymous reviewers for insightful comments and suggestions for
472 improving the manuscript.

473 **Competing interests**

474 The authors declare that they have no conflict of interest.

475 **Acknowledgments**

476 This work is supported by the Taiwan National Science and Technology Council grants NSTC-111-2121-M-008-
477 001 and NSTC-111-2111-M-008-030 and Taiwan Space Agency grant TASA-S-110316.

478 **Code and data availability**

479 The codes of the bias estimators used in this study are available at Github
480 (https://github.com/jiajia170801/bias_estimation_paper). The RO data is obtained from TDPC (TACC)
481 by https://tacc.cwb.gov.tw/data-service/fs7rt_tdpc/. The ECMWF reanalysis v5 (ERA5) data is
482 obtained from Copernicus server by [https://cds.climate.copernicus.eu/cdsapp#!/dataset/reanalysis-era5-
483 pressure-levels?tab=overview](https://cds.climate.copernicus.eu/cdsapp#!/dataset/reanalysis-era5-pressure-levels?tab=overview).

484

485 **References**

486 Anthes, R., Sjoberg, J., Feng, X., and Syndergaard, S.: Comparison of COSMIC and COSMIC-2 Radio
487 Occultation Refractivity and Bending Angle Uncertainties in August 2006 and 2021, *Atmosphere*, 13,
488 <https://doi.org/10.3390/atmos13050790>, 2022.

489 Ao, C., Chan, T., Iijima, B., Li, J., Mannucci, A., Teixeira, J., Tian, B., and Waliser, D.: Planetary boundary layer
490 information from GPS radio occultation measurements, GRAS SAF Workshop on Applications of GPSRO
491 Measurements, 123-131, 2008.

492 Bowler, N. E.: Revised GNSS-RO observation uncertainties in the Met Office NWP system, *Q. J. R. Meteorol.*
493 *Soc.*, 146, 2274-2296, <https://doi.org/10.1002/qj.3791>, 2020.

494 Bowler, N. E. : An assessment of GNSS radio occultation data produced by Spire, *Q. J. R. Meteorol. Soc.*, 146,
495 3772-3788, <https://doi.org/10.1002/qj.3872>, 2020.

496 Chang, C.-C. and Yang, S.-C.: Impact of assimilating Formosat-7/COSMIC-II GNSS radio occultation data on
497 heavy rainfall prediction in Taiwan, *Terr. Atmos. Ocean. Sci.*, 33, <https://doi.org/10.1007/s44195-022-00004-4>,
498 2022.

499 Chen, S.-Y., Kuo, Y.-H., and Huang, C.-Y.: The Impact of GPS RO Data on the Prediction of Tropical
500 Cyclogenesis Using a Nonlocal Observation Operator: An Initial Assessment, *Mon. Weather Rev.*, 148, 2701-
501 2717, [10.1175/mwr-d-19-0286.1](https://doi.org/10.1175/mwr-d-19-0286.1), 2020.

502 Chen, S.-Y., Shih, C.-P., Huang, C.-Y., and Teng, W.-H.: An Impact Study of GNSS RO Data on the Prediction
503 of Typhoon Nepartak (2016) Using a Multi-resolution Global Model with 3D-Hybrid Data Assimilation. *Weather*
504 *Forecast.*, 36, <https://doi.org/10.1175/waf-d-20-0175.1>, 2021a.

505 Chen, S.-Y., T.-C. Nguyen, and C.-Y. Huang: Impact of Radio Occultation Data on the Prediction of Typhoon
506 Haishen (2020) with WRFDA Hybrid Assimilation. *Atmosphere*, 12, 1397.
507 <https://doi.org/10.3390/atmos12111397>, 2021b.

508 Chen, S.-Y., Liu, C.-Y., Huang, C.-Y., Hsu, S.-C., Li, H.-W., Lin, P.-H., Cheng, J.-P., and Huang, C.-Y.: An
509 Analysis Study of FORMOSAT-7/COSMIC-2 Radio Occultation Data in the Troposphere, *Remote Sens.*, 13,
510 <https://doi.org/10.3390/rs13040717>, 2021c.

511 Chen, Y.-J., Hong, J.-S., and Chen, W.-J.: Impact of Assimilating FORMOSAT-7/COSMIC-2 Radio Occultation
512 Data on Typhoon Prediction Using a Regional Model, *Atmosphere*, 13, [10.3390/atmos13111879](https://doi.org/10.3390/atmos13111879), 2022.

513 Chien, F. C., Hong, J. S., and Kuo, Y. H.: The Marine Boundary Layer Height over the Western North Pacific
514 Based on GPS Radio Occultation, Island Soundings, and Numerical Models, *Sensor-Basel*, 19,
515 <https://doi.org/10.3390/s19010155>, 2019.

516 Clarizia, M. P., Ruf, C. S., Jales, P., and Gommenginger, C.: Spaceborne GNSS-R Minimum Variance Wind
517 Speed Estimator, *IEEE. T. Geosci. Remote*, 52, 6829-6843, <https://doi.org/10.1109/tgrs.2014.2303831>, 2014.

518 Cucurull, L.: Improvement in the Use of an Operational Constellation of GPS Radio Occultation Receivers in
519 Weather Forecasting, *Weather Forecast*, 25, 749-767, <https://doi.org/10.1175/2009waf2222302.1>, 2010.

520 Cucurull, L. and Mueller, M. J.: An Analysis of Alternatives for the COSMIC-2 Constellation in the Context of
521 Global Observing System Simulation Experiments, *Weather Forecast*, 35, 51-66, [https://doi.org/10.1175/waf-d-](https://doi.org/10.1175/waf-d-19-0185.1)
522 19-0185.1, 2020.

523 Cucurull, L., Li, R., and Peevey, T. R.: Assessment of Radio Occultation Observations from the COSMIC-2
524 Mission with a Simplified Observing System Simulation Experiment Configuration, *Mon. Weather Rev.*, 145,
525 3581-3597, <https://doi.org/10.1175/mwr-d-16-0475.1>, 2017.

526 Cucurull, L., Derber, J. C., Treadon, R., and Purser, R. J.: Assimilation of Global Positioning System Radio
527 Occultation Observations into NCEP's Global Data Assimilation System, *Mon. Weather Rev.*, 135, 3174-3193,
528 <https://doi.org/10.1175/mwr3461.1>, 2007.

529 Eyre, J.: Assimilation of radio occultation measurements into a numerical weather prediction system, ECMWF
530 Technical Memorandum, 34, <https://doi.org/10.21957/r8zjif4it>, 1994.

531 Feng, X., Xie, F., Ao, C. O., and Anthes, R. A.: Ducting and Biases of GPS Radio Occultation Bending Angle
532 and Refractivity in the Moist Lower Troposphere, *J. Atmos. Ocean. Tech.*, 37, 1013-1025,
533 <https://doi.org/10.1175/jtech-d-19-0206.1>, 2020.

534 Fertig, E. J., Hunt, B. R., Ott, E., and Szunyogh, I.: Assimilating non-local observations with a local ensemble
535 Kalman filter, *Tellus A*, 59, <https://doi.org/10.1111/j.1600-0870.2007.00260.x>, 2007.

536 Gorbunov, M. E.: Canonical transform method for processing radio occultation data in the lower troposphere,
537 *Radio Sci.*, 37, 9-1-9-10, <https://doi.org/10.1029/2000rs002592>, 2002.

538 Gorbunov, M. E. and Lauritsen, K. B.: Analysis of wave fields by Fourier integral operators and their application
539 for radio occultations, *Radio Sci.*, 39, <https://doi.org/10.1029/2003rs002971>, 2004.

540 Gorbunov, M. E., Vorob'ev, V. V., and Lauritsen, K. B.: Fluctuations of refractivity as a systematic error source
541 in radio occultations, *Radio Sci.*, 50, 656-669, <https://doi.org/10.1002/2014rs005639>, 2015.

542 Gorbunov, M. E., Lauritsen, K. B., Rhodin, A., Tomassini, M., and Kornbluh, L.: Radio holographic filtering,
543 error estimation, and quality control of radio occultation data, *J. Geophys. Res.-Atmos.*, 111,
544 <https://doi.org/10.1029/2005jd006427>, 2006.

545 Healy, S. B.: Forecast impact experiment with a constellation of GPS radio occultation receivers, *Atmos. Sci.*
546 *Lett.*, 9, 111-118, <https://doi.org/10.1002/asl.169>, 2008.

547 Healy, S.: Assimilation in the upper-troposphere and lower-stratosphere: The role of GPS radio occultation,
548 Seminar on Use of Satellite Observations in Numerical Weather Prediction, Shinfield Park, Reading, 2014.

549 Hsu, S. A.: Coastal Meteorology, *Encyclopedia of Physical Science and Technology (Third Edition)*, 155-173,
550 2003.

551 Jensen, A. S., Lohmann, M. S., Benzon, H.-H., and Nielsen, A. S.: Full Spectrum Inversion of radio occultation
552 signals, *Radio Sci.*, 38, <https://doi.org/10.1029/2002rs002763>, 2003.

553 Jensen, A. S., Lohmann, M. S., Nielsen, A. S., and Benzon, H.-H.: Geometrical optics phase matching of radio
554 occultation signals, *Radio Sci.*, 39, <https://doi.org/10.1029/2003rs002899>, 2004.

555 Jensen, A. S., Benzon, H.-H., Nielsen, A. S., Marquardt, C., and Lohmann, M. S.: Evaluation of the Processing
556 of Radio Occultation Signals by Reconstruction of the Real Signals, in: *Atmosphere and Climate: Studies by*
557 *Occultation Methods*, edited by: Foelsche, U., Kirchengast, G., and Steiner, A., Springer Berlin Heidelberg, Berlin,
558 Heidelberg, 113-125, https://doi.org/10.1007/3-540-34121-8_10, 2006.

559 Kuo, Y.-H., Wee, T.-K., Sokolovskiy, S., Rocken, C., Schreiner, W., Hunt, D., and Anthes, R. A.: *J. Meteorol.*
560 *Soc. Jpn.*, 82, 507–531, <https://doi.org/10.2151/jmsj.2004.507>, 2004.

561 Lien, G.-Y., Lin, C.-H., Huang, Z.-M., Teng, W.-H., Chen, J.-H., Lin, C.-C., Ho, H.-H., Huang, J.-Y., Hong, J.-
562 S., Cheng, C.-P., and Huang, C.-Y.: Assimilation Impact of Early FORMOSAT-7/COSMIC-2 GNSS Radio
563 Occultation Data with Taiwan’s CWB Global Forecast System, *Mon. Weather Rev.*, [https://doi.org/10.1175/mwr-](https://doi.org/10.1175/mwr-d-20-0267.1)
564 [d-20-0267.1](https://doi.org/10.1175/mwr-d-20-0267.1), 2021.

565 Liu, H., Kuo, Y. H., Sokolovskiy, S., Zou, X., and Zeng, Z.: Analysis bias induced in assimilation of the radio
566 occultation bending angle with complex structures in the tropical troposphere, *Q. J. R. Meteorol. Soc.*, 146, 4030-
567 4037, <https://doi.org/10.1002/qj.3887>, 2020.

568 Liu, H., Kuo, Y.-H., Sokolovskiy, S., Zou, X., Zeng, Z., Hsiao, L.-F., and Ruston, B. C.: A Quality Control
569 Procedure Based on Bending Angle Measurement Uncertainty for Radio Occultation Data Assimilation in the
570 Tropical Lower Troposphere, *J. Atmos. Ocean. Tech.*, 35, 2117-2131, <https://doi.org/10.1175/jtech-d-17-0224.1>,
571 2018.

572 Rennie, M. P.: The impact of GPS radio occultation assimilation at the Met Office, *Q. J. R. Meteorol. Soc.*, 136,
573 116-131, <https://doi.org/10.1002/qj.521>, 2010.

574 Rocken, C., Anthes, R., Exner, M., Hunt, D., Sokolovskiy, S., Ware, R., Gorbunov, M., Schreiner, W., Feng, D.,
575 Herman, B., Kuo, Y. H., and Zou, X.: Analysis and validation of GPS/MET data in the neutral atmosphere, *J.*
576 *Geophys. Res.-Atmos.*, 102, 29849-29866, <https://doi.org/10.1029/97jd02400>, 1997.

577 **Sjoberg, J., R.A. Anthes and H. Zhang, 2023: Estimating individual radio occultation uncertainties**
578 **using the observations and environmental parameters. *J. Atmos. and Ocean Tech.*, 40 (accepted for**
579 **publication 8-28-23).**

580 Schreiner, W., Sokolovskiy, S., Hunt, D., Rocken, C., and Kuo, Y. H.: Analysis of GPS radio occultation data
581 from the FORMOSAT-3/COSMIC and Metop/GRAS missions at CDAAC, *Atmos. Meas. Tech.*, 4, 2255-2272,
582 <https://doi.org/10.5194/amt-4-2255-2011>, 2011.

583 Schreiner, W. S., Weiss, J. P., Anthes, R. A., Braun, J., Chu, V., Fong, J., Hunt, D., Kuo, Y. H., Meehan, T.,
584 Serafino, W., Sjoberg, J., Sokolovskiy, S., Talaat, E., Wee, T. K., and Zeng, Z.: COSMIC-2 Radio Occultation
585 Constellation: First Results, *Geophys. Res. Lett.*, 47, <https://doi.org/10.1029/2019gl086841>, 2020.

586 Sokolovskiy, S.: Effect of superrefraction on inversions of radio occultation signals in the lower troposphere,
587 *Radio Sci.*, 38, <https://doi.org/10.1029/2002rs002728>, 2003.

588 Sokolovskiy, S., Rocken, C., Schreiner, W., and Hunt, D.: On the uncertainty of radio occultation inversions in
589 the lower troposphere, *J. Geophys. Res.*, 115, <https://doi.org/10.1029/2010jd014058>, 2010.

590 Sokolovskiy, S., W. Schreiner, Z. Zeng, D. Hunt, Y.-C. Lin, and Y.-H. Kuo (2014), Observation, analysis, and
591 modeling of deep radio occultation signals: Effects of tropospheric ducts and interfering signals, *Radio Sci.*, 49,
592 954–970, doi:10.1002/2014RS005436.

593 Tatarskiy, V. I.: Determining atmospheric density from satellite phase and refraction-angle measurements, *Izv.*
594 *Atmos. Oceanic Phys.*, 4, 401-406, 1968.

595 Wang, K.-N., Ao, C., and de la Torre Juárez, M.: GNSS-RO Refractivity Bias Correction Under Ducting Layer
596 Using Surface-Reflection Signal, *Remote Sens.*, 12, <https://doi.org/10.3390/rs12030359>, 2020.

597 Wang, K.-N., de la Torre Juárez, M., Ao, C. O., and Xie, F.: Correcting negatively biased refractivity below ducts
598 in GNSS radio occultation: an optimal estimation approach towards improving planetary boundary layer (PBL)
599 characterization, *Atmos. Meas. Tech.*, <https://doi.org/10.4761-4776.10.5194/amt-10-4761-2017>, 2017.

600 Wee, T. K. and Kuo, Y. H.: A perspective on the fundamental quality of GPS radio occultation data, *Atmos. Meas.*
601 *Tech.*, 8, 4281-4294, <https://doi.org/10.5194/amt-8-4281-2015>, 2015.

602 Wee, T.-K.: A variational regularization of Abel transform for GPS radio occultation, *Atmos. Meas. Tech.*, 11,
603 1947–1969, <https://doi.org/10.5194/amt-11-1947-2018>, 2018.

604 Xie, F., Syndergaard, S., Kursinski, E. R., and Herman, B. M.: An Approach for Retrieving Marine Boundary
605 Layer Refractivity from GPS Occultation Data in the Presence of Superrefraction, *J. Atmos. Ocean. Tech.*, 23,
606 1629-1644, <https://doi.org/10.1175/JTECH1996.1>, 2006.

607 Xie, F., Wu, D. L., Ao, C. O., Kursinski, E. R., Mannucci, A. J., and Syndergaard, S.: Super-refraction effects on
608 GPS radio occultation refractivity in marine boundary layers, *Geophys. Res. Lett.*, 37,
609 <https://doi.org/10.1029/2010gl043299>, 2010.

610 Xie, F, *Visiting Scientist Report 21: Investigation of methods for the determination of the PBL height from RO*
611 *observations using ECMWF reanalysis data, SAF/ROM/DMI/REP/VS21/001, 2014.*

612 Yang, J., Wang, Z., Heymsfield, A. J., and French, J. R.: Characteristics of vertical air motion in isolated
613 convective clouds, *Atmos. Chem. Phys.*, 16, 10159-10173, <https://doi.org/10.5194/acp-16-10159-2016>, 2016.

614 Yang, S.-C., Chen, S.-H., Chen, S.-Y., Huang, C.-Y., and Chen, C.-S.: Evaluating the Impact of the COSMIC RO
615 Bending Angle Data on Predicting the Heavy Precipitation Episode on 16 June 2008 during SoWMEX-IOP8,
616 *Mon. Weather Rev.*, 142, 4139-4163, <https://doi.org/10.1175/mwr-d-13-00275.1>, 2014.

617 Zhang, H., Kuo, Y.-H., and Sokolovskiy, S.: Assimilation of Radio Occultation Data Using Measurement-Based
618 Observation Error Specification: Preliminary Results, *Mon. Weather Rev.*, 151, 589-601,
619 <https://doi.org/10.1175/mwr-d-22-0122.1>, 2023.

620

621 **Table 1: Correlation coefficients between the mean real and estimated REFBs below 1.5 km over ocean and**
 622 **land in Southern Hemisphere (SH) and Northern Hemisphere**

Correlation coefficients	LSW based		<i>TQ</i> based	
	Ocean (SH/NH)	Land (SH/NH)	Ocean (SH/NH)	Land (SH/NH)
Training data set	0.94/0.96	0.9/0.92	0.79/0.75	0.72/0.69
Testing data set	0.93/0.96	0.89/0.87	0.71/0.68	0.70/0.63

623

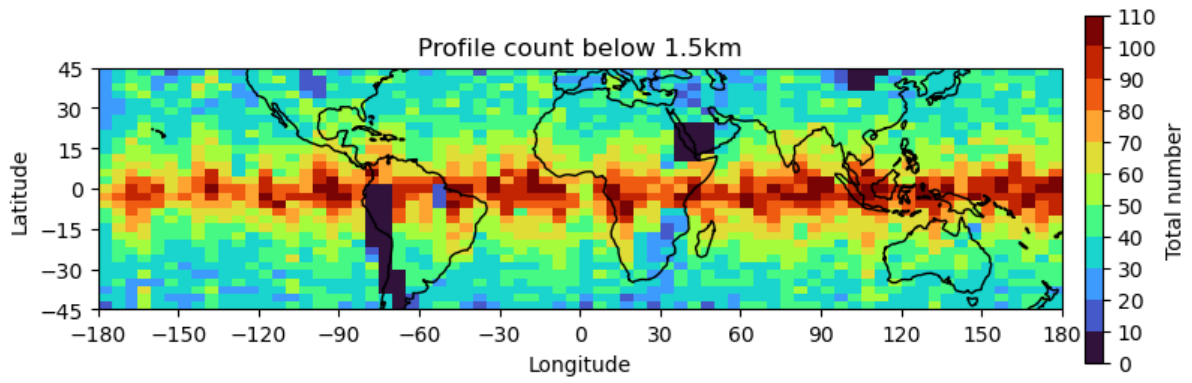
624

625 **Table 2: Global mean RMSE of each REFB estimation in comparison to the real REFB below 1.5 km**

Global mean RMSE	LSW-based	<i>TQ</i> -based	MVE
Training data set	2.033	1.614	1.088
Testing data set	2.815	2.266	1.731

626

627

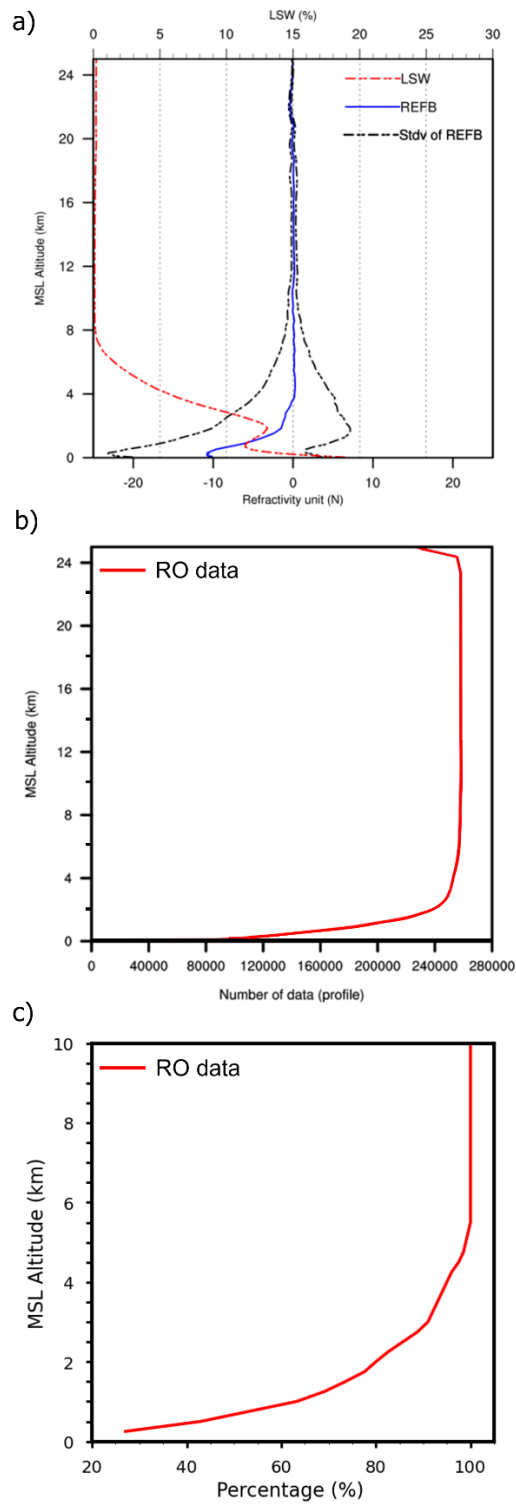


628

629 **Figure 1: Number** of FS7/C2 RO profiles below the 1.5 km height during the study period (unit: number of profiles).

630

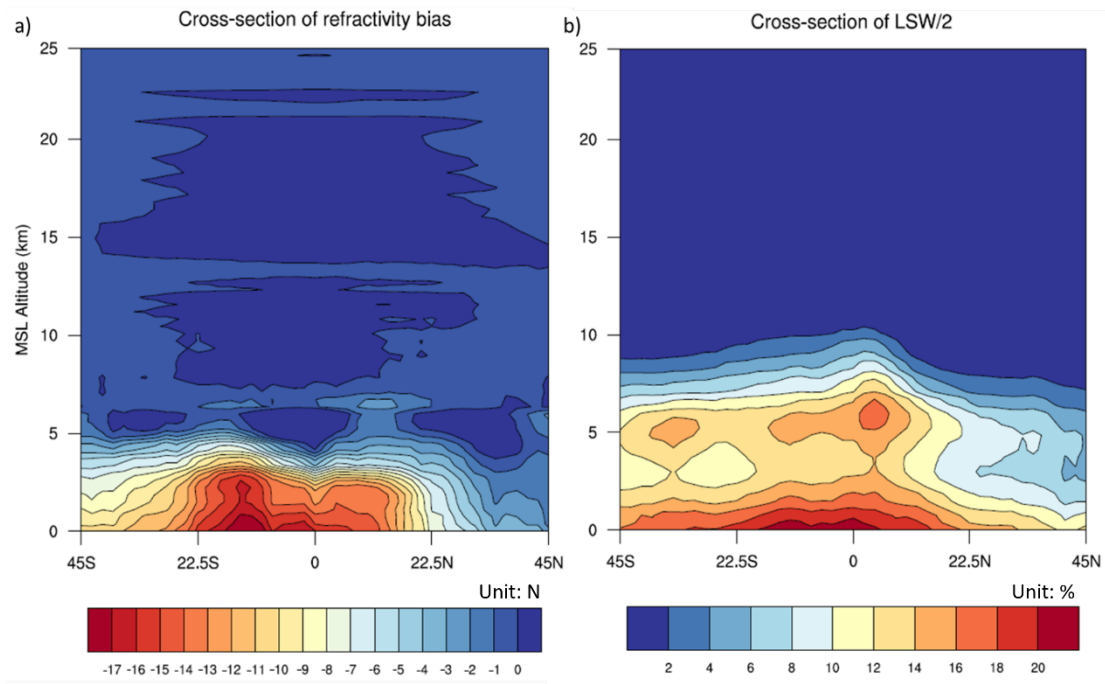
631



632

633 **Figure 2: (a) Mean and standard deviation of REFB and mean LSW as a function of height. (b) The amount of available**
 634 **RO data, and (c) the percentage of profiles as a function of height in reference to the total number at 10 km. The RO**
 635 **data are from 1st December 2019 to 29th February 2020.**

636



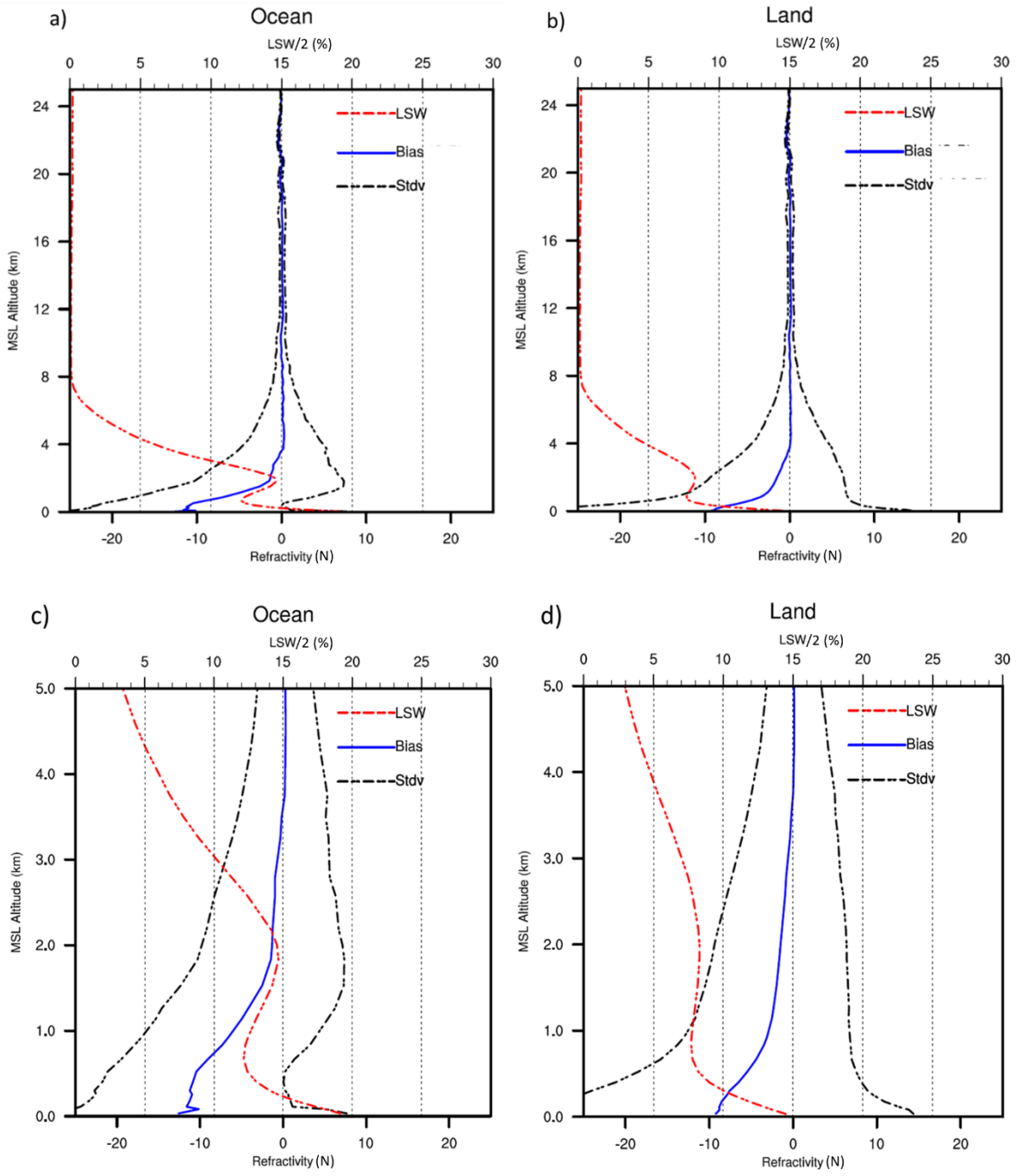
637

638

639

640

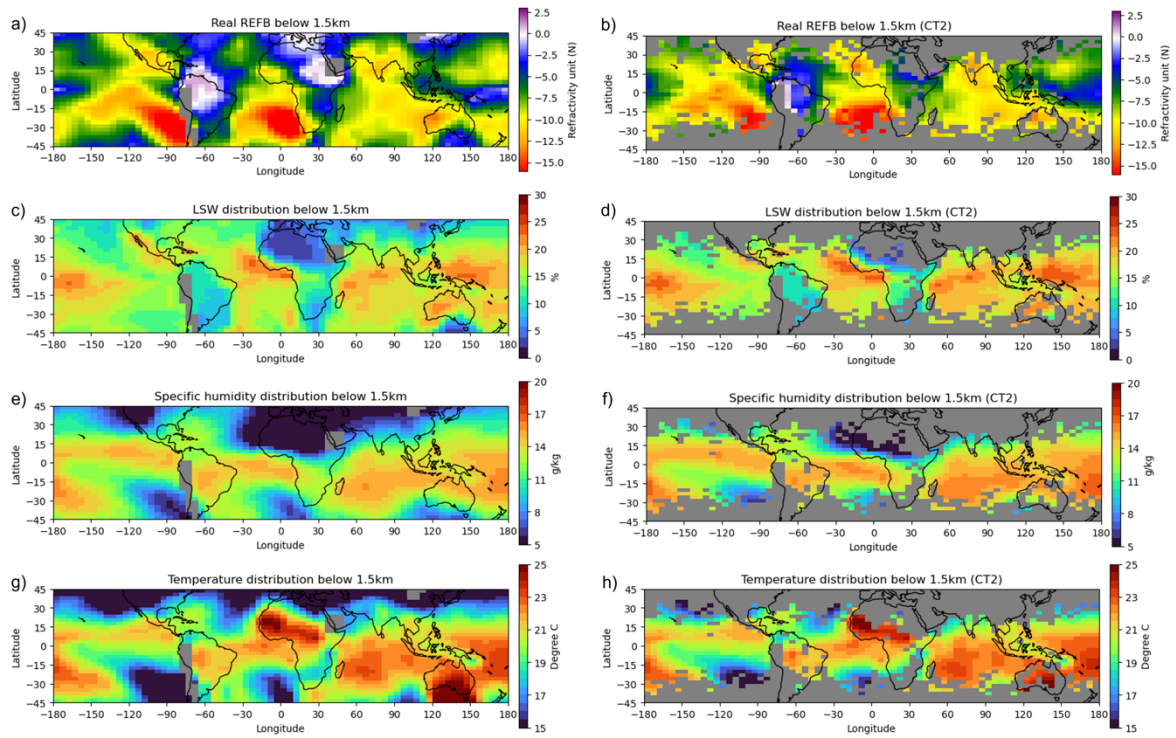
Figure 3: The cross-sections of (a) zonal mean REFB and (b) mean LSW/2 from 1st December 2019 to 29th February 2020.



641

642 **Figure 4: (a) and (b) are vertical profiles of the mean and standard deviation of REF B, and mean LSW with altitudes**
 643 **up to 25 km over ocean and land, respectively. (c) and (d) are the same as (a) and (b) except zoomed versions below 5**
 644 **km.**

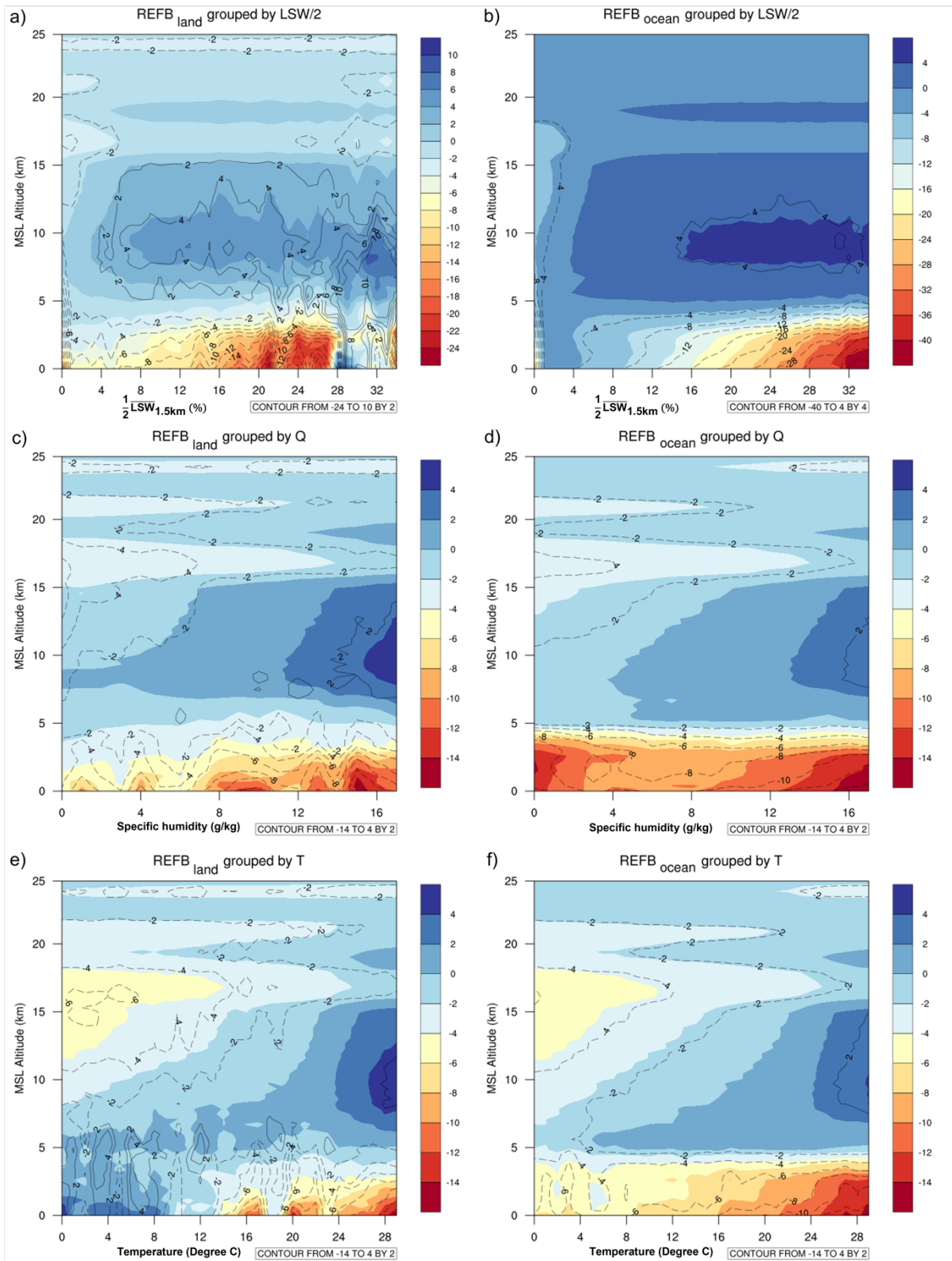
645



646

647 **Figure 5: Horizontal distribution of (a) REFB (N units), (c) LSW (%), (e) specific humidity ($g\ kg^{-1}$), and (g) temperature**
 648 **($^{\circ}C$) during the study period. The values of REFB, LSW, specific humidity and temperature are averages over the**
 649 **lowest 1.5 km MSL of the atmosphere. (b), (d), (f) and (h) are the same as (c), (c), (e) and (g), but they are calculated**
 650 **with the criterion that at least 30 profiles penetrate below 0.5 km in each box.**

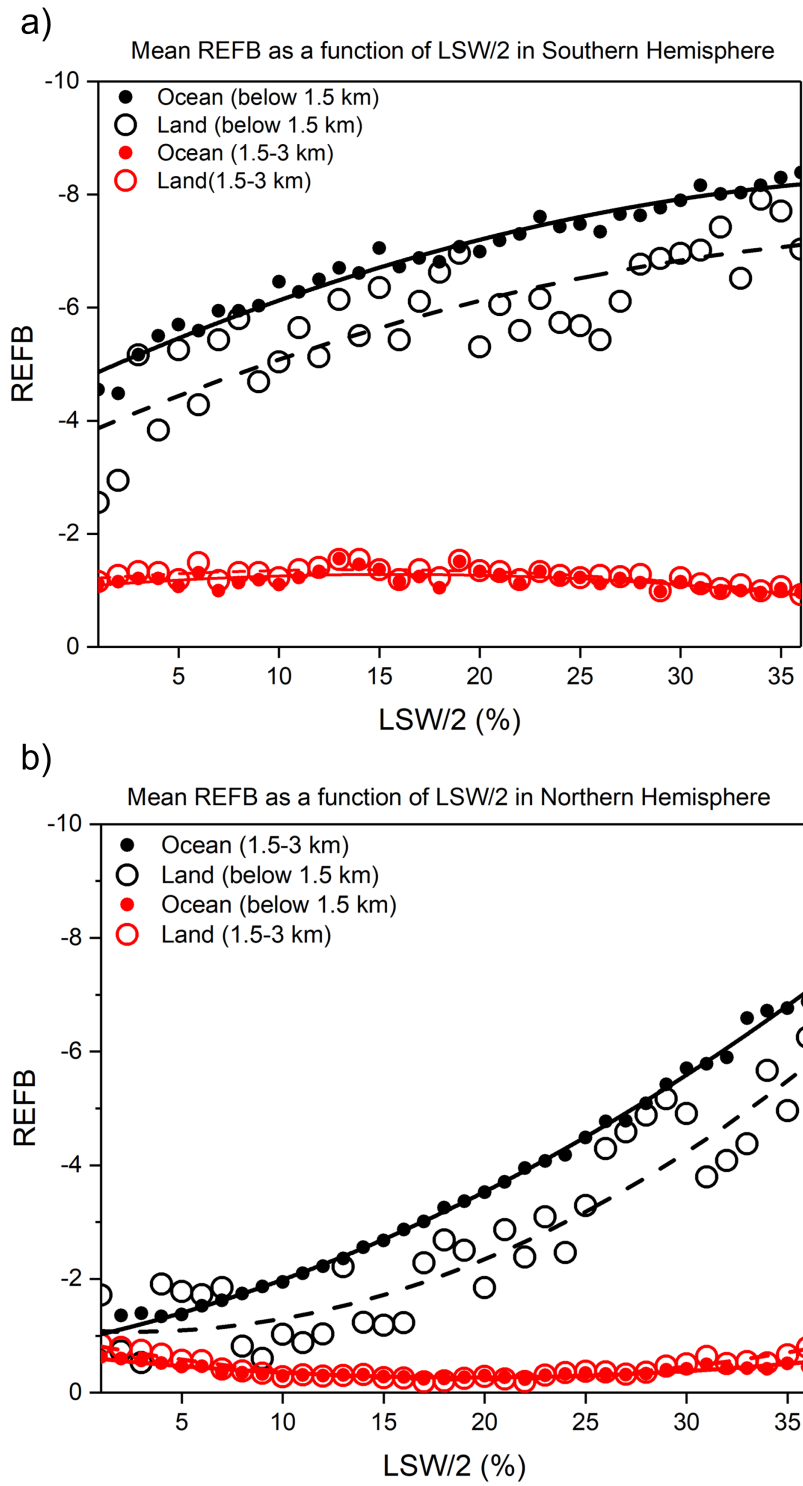
651



652

653 **Figure 6: Refractivity bias as a function of height and average values over the lowest 1.5 km above MSL of (a) LSW/2,**
 654 **(c) specific humidity and (e) temperature over land. (b), (d) and (f) are the same as (a), (c) and (e), except over the ocean.**
 655 **The color shading shows the result using the RO profiles penetrating below 1.5 km while the contour uses the RO**
 656 **profiles penetrating below 0.5 km.**

657



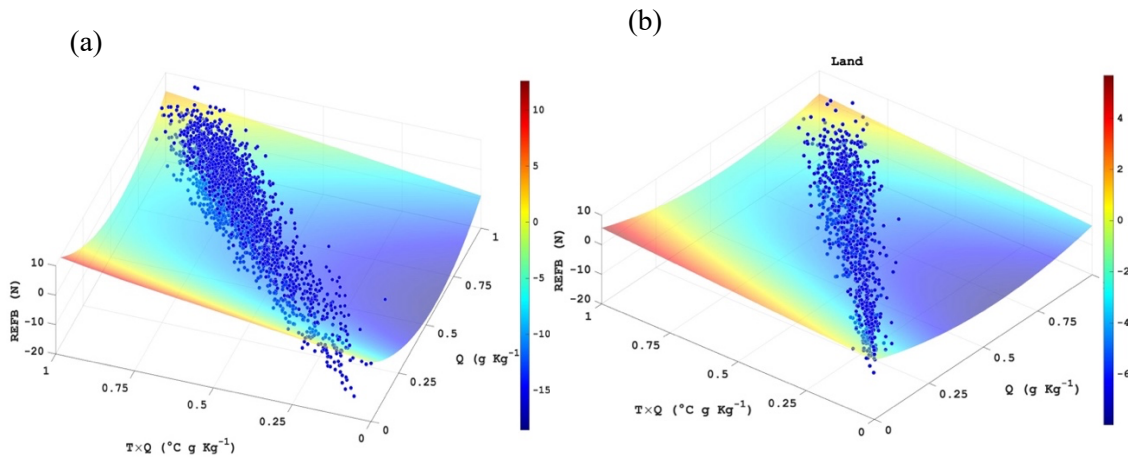
658

659 **Figure 7: Relationship between LSW/2 and REFB. The solid and dashed lines represent the REFB computed from the**
 660 **statistical model for the ocean and land, respectively, as a function of LSW/2 (Southern Hemisphere only). LSW/2 and**
 661 **REFB are averaged below 1.5 km.**

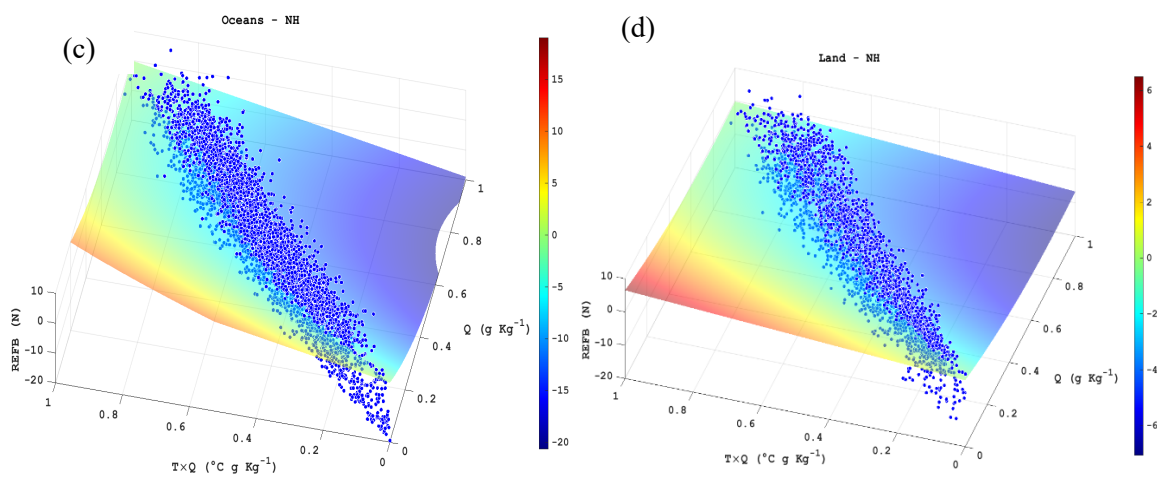
662

663

664



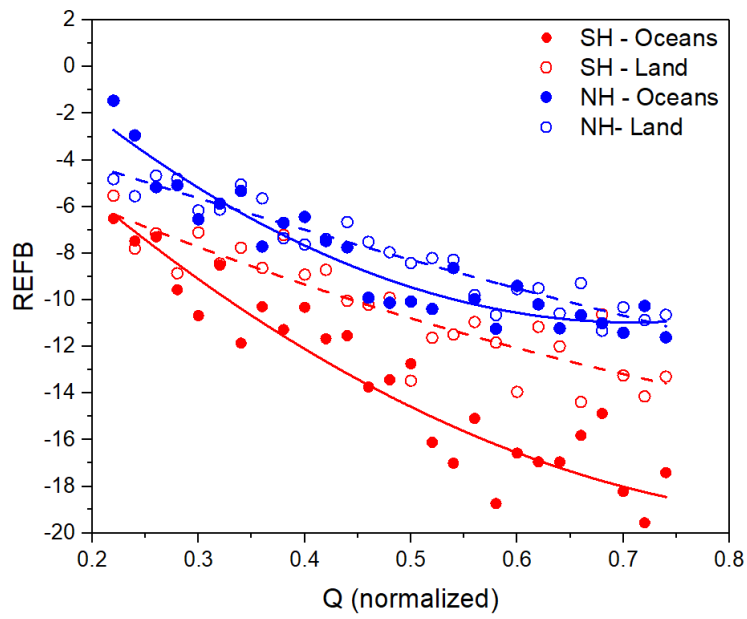
665



666

667 **Figure 8: The relationship among REFB, normalized specific humidity, product of normalized temperature and**
668 **normalized specific humidity of a) oceans and b) land in the Southern Hemisphere. The scatters are the averaged values**
669 **of each profile below the lowest 1.5 km MSL. The surfaces show the model computed from statistical model (Eq. 3) as**
670 **the function of normalized specific humidity and product of normalized temperature and humidity. (c) and (d) are the**
671 **same as (a) and (b), but for the Northern Hemisphere.**

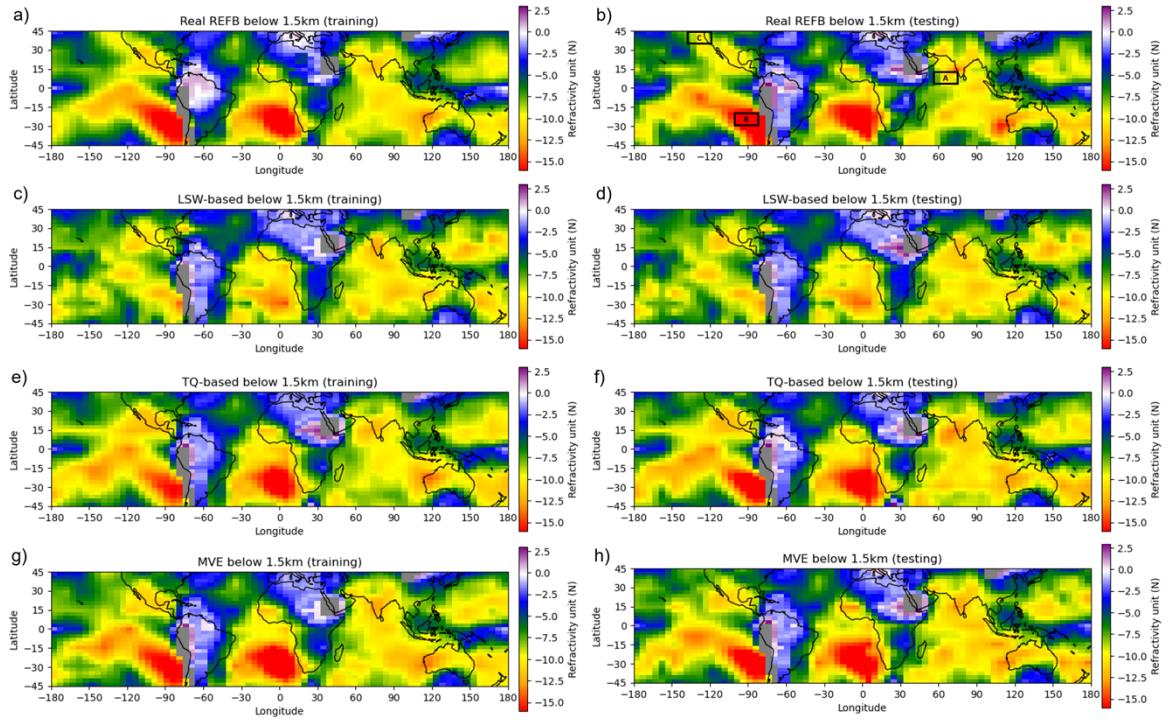
672



673

674 **Figure 9: The relationship between REFB and normalized Q given a condition of normalized $TQ=0.5$.**

675



676

677

678

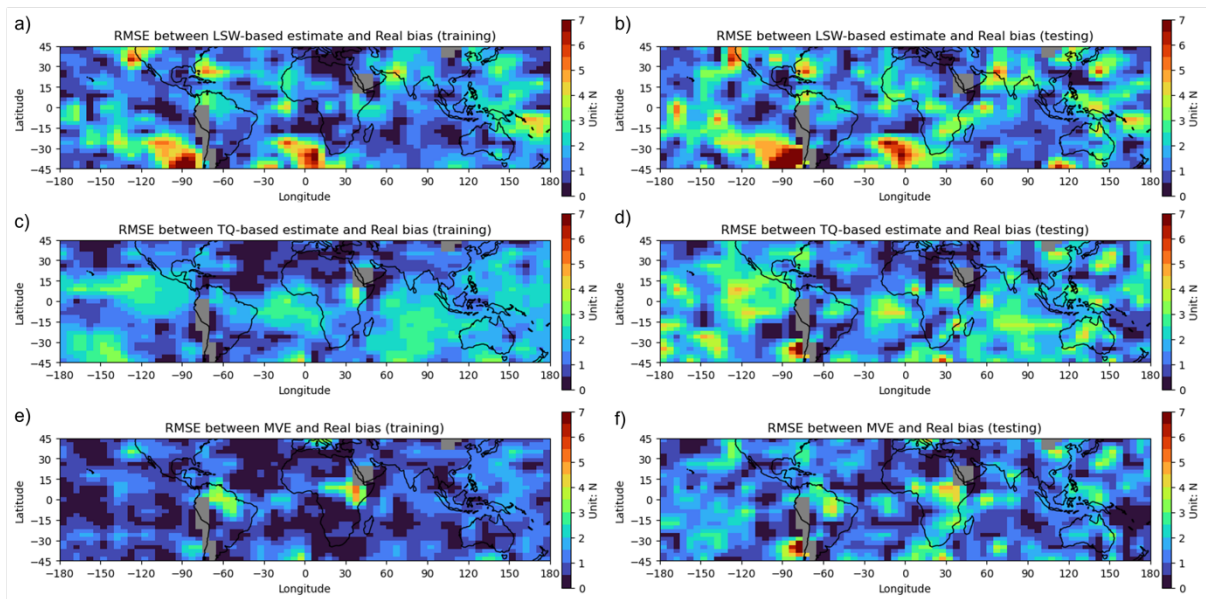
679

680

681

Figure 10: Horizontal distribution of refractivity bias and different estimated refractivity biases. The boxes denoted A and B are the example boxes used in Figures 12 and 13, respectively. **All variables used to construct this figure are averaged below 1.5km. Area A is in the region of $0^{\circ} < \text{Lat} < 10^{\circ}\text{N}$ and $55^{\circ}\text{E} < \text{Lon} < 75^{\circ}\text{E}$, Area B is in the region of $20^{\circ}\text{S} < \text{Lat} < 30^{\circ}\text{S}$ and $105^{\circ}\text{W} < \text{Lon} < 85^{\circ}\text{W}$, and Area C is in the region of $35^{\circ}\text{S} < \text{Lat} < 45^{\circ}\text{S}$ and $120^{\circ}\text{W} < \text{Lon} < 135^{\circ}\text{W}$.**

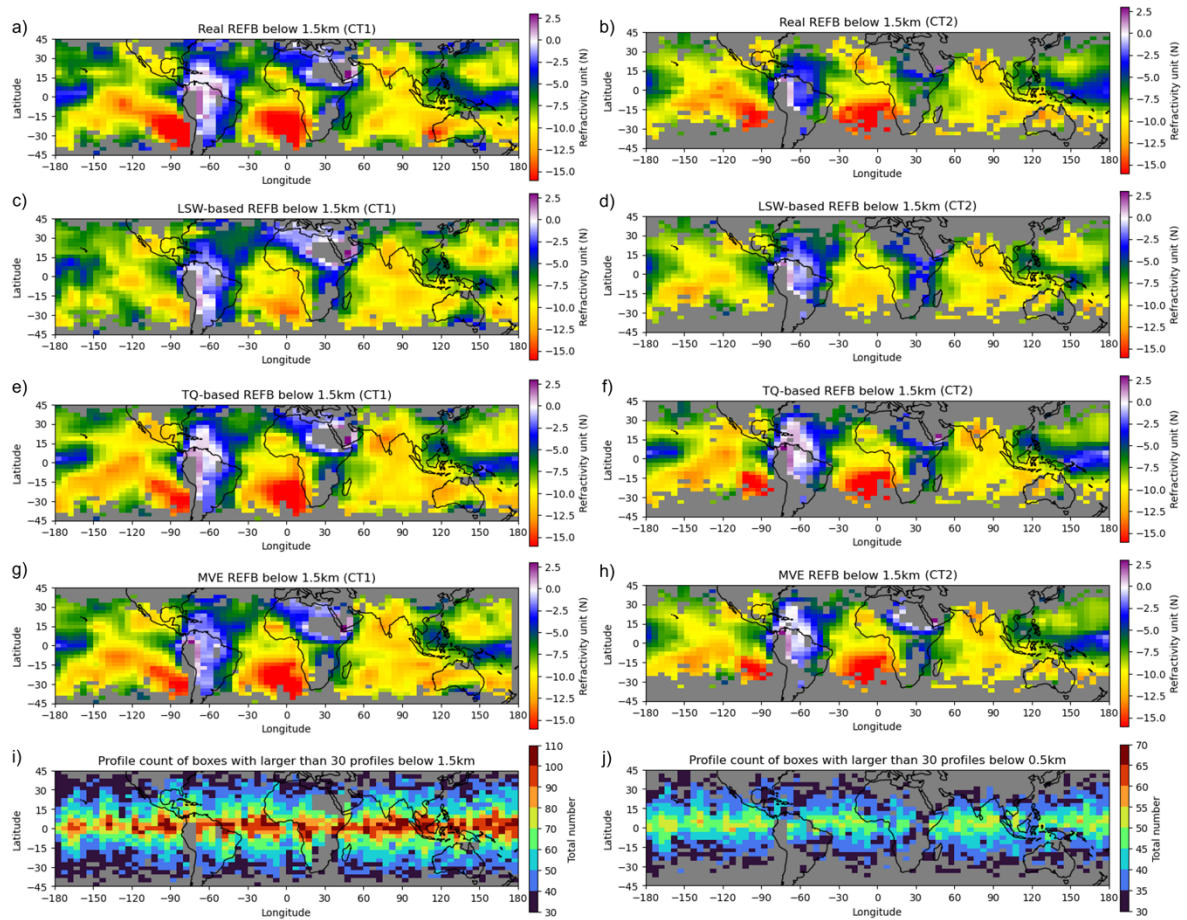
682



683

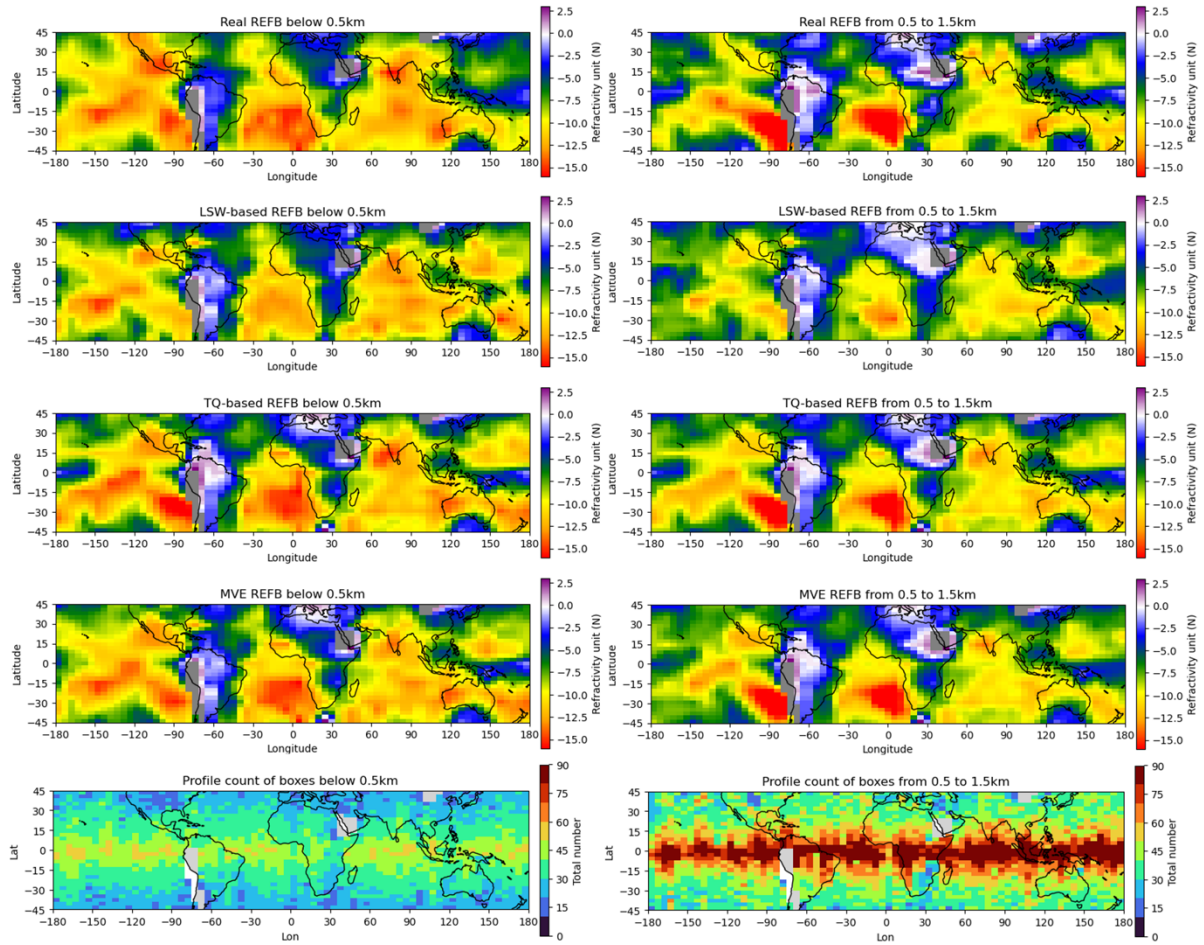
684 **Figure 11:** Horizontal distribution of RMSE between the real REFB and estimated REFB by different methods with
685 training (left column) and testing (right column) data.

686



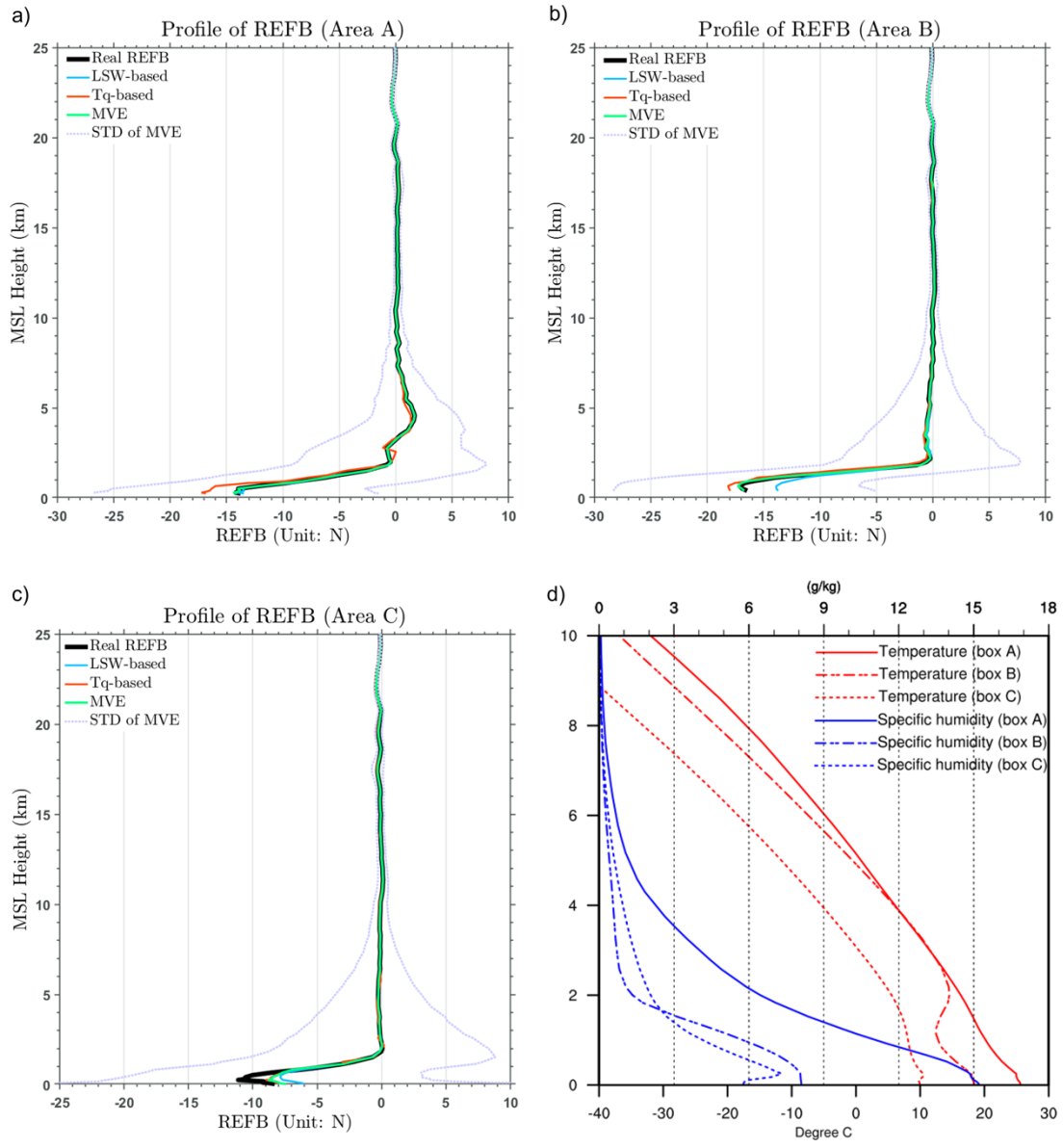
687

688 **Figure 12: The same as Fig. 10, but the calculation is done for RO data with different criteria (CT1 and CT2) of sample**
 689 **selection. CT1 requires at least 30 RO profiles penetrate below 1.5 km in each box, and CT2 is the same as CT2 except**
 690 **that the profiles penetrate 0.5 km. (i) and (j) are the horizontal distribution of the profile count with criterion CT1 and**
 691 **CT2, respectively.**



692

693 **Figure 13: The same as Fig. 10, but the calculation is done for RO data from different levels. The left column uses the**
 694 **data below 0.5 km and the right column use the data between 0.5 and 1.5 km. (i) and (j) are the horizontal distribution**
 695 **of the profile count below 0.5km and between 0.5 and 1.5 km, respectively.**



696 **Figure 14: Profiles of refractivity bias (real and estimates) for two different areas selected in Fig. 10a. Boxes A, B and**
 697 **C are in ($0^\circ < \text{Lat} < 10^\circ\text{N}$, $55^\circ\text{E} < \text{Lon} < 75^\circ\text{E}$) and ($20^\circ\text{S} < \text{Lat} < 30^\circ\text{S}$, $105^\circ\text{W} < \text{Lon} < 85^\circ\text{W}$) and ($35^\circ\text{S} < \text{Lat} < 45^\circ\text{S}$**
 698 **and $120^\circ\text{W} < \text{Lon} < 135^\circ\text{W}$). (d) Profiles of temperature (red lines) and specific humidity (blue lines) averaged for**
 699 **Areas A (solid lines), B (long-dashed lines) and C (short-dashed line) shown in Fig. 10b.**

700

701

